# A simple impedance-infinite element for the finite element solution of the three-dimensional wave equation in unbounded domains

Loukas F. Kallivokas[a], Jacobo Bielak[a,*], Richard C. MacCamy[b]

[a]*Computational Mechanics Laboratory, Department of Civil and Environmental Engineering, Pittsburgh, PA 15213-3890, USA*
[b]*Department of Mathematical Sciences, Carnegie Mellon University, Pittsburgh, PA 15213, USA*

**Abstract**

This paper is concerned with the development of an efficient and accurate impedance-infinite element that can be used either in the frequency- or directly in the time-domain for the modeling and solution of problems described by the scalar three-dimensional wave equation in infinite or semi-infinite domains. The infinite domain is truncated and the effect of the truncated infinite region is simulated by the introduction of an absorbing boundary condition prescribed on the truncation boundary. A systematic procedure for the construction of a family of such conditions of increasing accuracy and complexity is developed with explicit formulas given for approximations up to second order. A central feature of this high-order approximation is that it can be expressed, within the context of a finite element formulation, as a set of local infinite elements located at the boundary of the computational domain, with each element defined by a pair of symmetric, time-invariant, stiffness and damping matrices. This makes it possible to incorporate readily the new local boundary element into finite element software developed for purely interior regions, for applications involving steady-state harmonic or transient excitations. Whereas the theory has been developed formally for arbitrary smooth boundary surfaces, here details are provided for ellipsoidal and spherical boundaries. Thus far, only the latter has been implemented and tested in problems involving cavities and rigid scatterers of spherical and cubic shape. Numerical experiments in both the frequency- and time-domain attest to the efficacy and accuracy of the proposed new element.

## 1. Introduction

In many applications in mechanics and engineering there is often interest in studying radiation and scattering problems that arise when a structure interacts with a surrounding medium of infinite or semi-infinite extent. The exterior structural acoustics problem has been often used as a prototype situation; it typically involves a structure submerged in an unbounded, linear, compressible and inviscid fluid. Here, one is interested in determining the pressure field within the fluid and the displacement and stress field within the structure. One difficulty with radiation and scattering problems which is absent in those defined over bounded regions, is that the solution to the equations of motion that govern the behavior of the fluid–structure system must also satisfy a radiation condition. This requirement can represent a considerable complication.

One common approach for seeking numerical solutions to the problem is by well-known boundary integral representations; the solution within the infinite medium is expressed via integrals which involve the Cauchy data and appropriate Green's functions only along the boundary of the domain. The

---

* Corresponding author.

primary advantages of this methodology are: (a) reduction of the dimensionality of the problem, since, in the absence of sources within the infinite medium, only the interface and the structure need be discretized, and (b) a priori satisfaction of the radiation condition via the fundamental solutions that are embedded in the formulation. The disadvantages are the nonlocality of the resulting discretized equations and the difficulty of extending the formulation to nonlinear problems.

Alternative domain discretization methods such as the traditional finite element method lead, by contrast, to local equations in space and time and are able to handle nonlinearities quite readily. The finite element method, however, has an inherent difficulty in modeling infinite domains. It requires that the infinite medium be truncated through the introduction of an artificial boundary in order to render the domain finite. Solutions are then sought within the resulting finite region. Appropriate boundary conditions need to be devised on the artificial boundary that will simulate the radiation condition. There is a theoretically exact condition on the artificial boundary which is tantamount to a boundary integral formulation, but this is nonlocal in both time and space and difficult to determine and use. Hence, the effort is in devising approximate conditions that will retain most of the properties of the exact condition, while relaxing the spatial and/or temporal nonlocalities. The earliest and simplest condition devised for this purpose is the well-known plane-wave approximation (PWA) developed by Mindlin and Bleich [29]; it is an early-time (high-frequency) approximation that requires a fairly large computational domain for reasonable accuracy, especially at low dominant frequencies of excitation. Absorbing boundaries of a higher order of accuracy than the earlier PWA, have been proposed by a number of authors. A survey of various absorbing boundary treatments up to 1991 is given by Givoli [16]. Here, we mention the well-known sequences of boundary conditions derived by Engquist and Majda [9,10] and Bayliss and Turkel [3]. There are similarities, indeed equivalence in some instances, between various conditions; Kausel [26], for instance, showed that several absorbing conditions can be seen as members of the same family of absorbing boundaries developed by Engquist and Majda [9,10]. Various implementations of the Bayliss and Turkel's conditions in the time- and frequency-domains have been presented, e.g. in [1,6,31–33].

An inherent difficulty with the development of absorbing boundary conditions is the need to ensure the stability of the conditions and their validity for the low end of the frequency spectrum; they are usually well-behaved at the high-frequency end. In the 1970s, Geers [12], by combining the early- and late-time approaches, derived doubly asymptotic approximations (DAAs), an alternative to absorbing boundary conditions, which are exact in both the low- and high-frequency limits, local in time, but nonlocal in space. Improved versions have been developed more recently by Felippa [11], Geers and Felippa [14], and Nicolas-Vuillerme [30]. Due to their satisfactory accuracy even when placed directly on or in the proximity of the scatterer, DAAs have been used to solve fluid-shell systems of various degrees of complexity and have been implemented into several structure–fluid codes [8]. The price one pays for this benefit, however, is having to deal with a spatially nonlocal boundary, since at each instant DAAs couple the response at each point of the artificial boundary with that at every other point. Extensions to problems with inelastic interior structures using DAAs failed [13]. A different nonlocal treatment, based on the DtN approach [15] for time-harmonic problems, has recently been used with Galerkin/least-squares finite elements [18].

We remark that, within the context of the finite element method, devising absorbing boundary conditions and later coupling the conditions to the domain discretization scheme is only one of possible paths for tackling the appropriate treatment of the radiation condition. An alternative approach is via infinite elements, an idea pioneered by Zienkiewicz and Bettess [34]. In this approach, decay functions that describe the asymptotic behavior of the exact solutions are used at the truncation boundary and special elements, approximately called infinite, are devised, on which the decay functions are mapped. Bettess and Bettess [4,5] have recently reported on various infinite elements for both static and dynamic problems. The advantage of the infinite elements is their natural coupling to the interior finite elements; their drawback is that they are limited to frequency-domain formulations.

In this paper we adopt the idea of artificial boundaries and present a methodology that addresses two main issues, namely, the development of a family of stable absorbing boundary conditions and their efficient numerical treatment within the context of finite elements. We attempt to overcome some of the drawbacks of past developments by aiming at (a) developing and using a high-order condition that will

provide sufficient accuracy for engineering applications, (b) locality in time so that extensive storage of time histories is avoided and the resulting equations of motion can be easily integrated in time, (c) locality in space such that standard finite element techniques that preserve the symmetry and the sparsity of the overall system of equations may be used, (d) providing a finite element formulation that can be applied equally well in either the frequency- or directly in the time-domain.

The present development of the conditions for general three-dimensional problems builds on ideas developed earlier for one and two dimensions [2]. We remark that our three-dimensional conditions, in their initial form and despite their different point of departure, bear similarities to other conditions, most notably those developed by Bayliss and Turkel [3] for particular geometries (spherical). The numerical treatment of the absorbing boundary conditions borrows from similar ideas developed for two dimensions [21,22,23] within the context of finite element formulations. In particular, it is shown that, by virtue of a simple decomposition scheme suggested by the theory of viscoelasticity, a second-order condition is equivalent, upon discretization, to a pair of symmetric, frequency-independent, damping and stiffness matrices local to the artificial boundary. The latter pair of matrices, for which we provide closed-form expressions, essentially gives rise to an impedance-infinite element on the artificial boundary that can be employed for problems in either the time- or the frequency-domains.

The lack of truly transient accurate absorbing boundary conditions in three dimensions has been identified in the review articles already mentioned [4,5,16]; this paper aspires to fill that gap by presenting a systematic procedure for developing the conditions and a particular way by which they can be easily incorporated into existing finite element codes. A number of numerical examples for radiation and scattering problems including transient and harmonic steady-state excitations attest to the efficacy of the proposed methodology.

## 2. The exterior initial and boundary value problem for the wave equation

Let $\Gamma$ be a closed surface with exterior $\Omega \subset \mathfrak{R}^3$ (Fig. 1(a)). $\Omega$ is occupied by a linear, inviscid, and compressible fluid. We consider the radiation problem in which $\Gamma$ is subjected to a prescribed velocity. Let us state the mathematical problem; physical details are given, e.g. in [28].

Find $p(x, t)$ such that

$$\ddot{p}(x, t) = c^2 \Delta p(x, t) , \quad x \in \Omega , \quad t \geq 0 , \tag{1a}$$

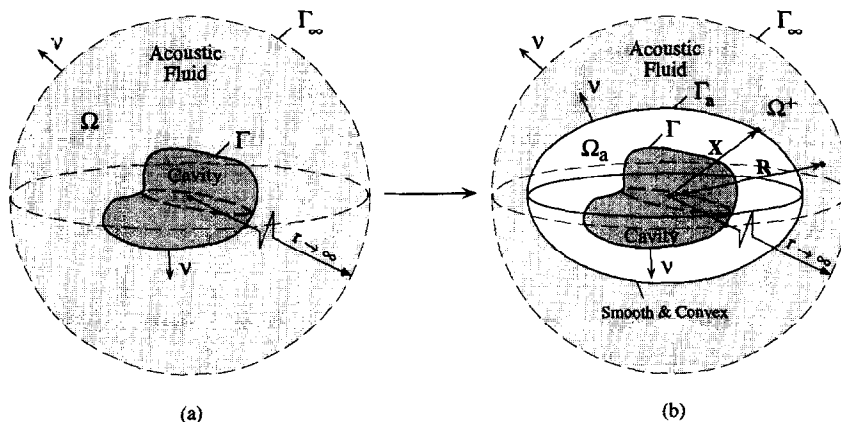$$p_\nu(x, t) = f_N(x, t) , \quad x \in \Gamma , \quad t > 0 , \tag{1b}$$



Fig. 1. (a) Model of cavity surrounded by infinite acoustic fluid; (b) reduced model with finite fluid region $\Omega_a$ and absorbing boundary.

$$\lim_{r \to \infty} r\left(p_r + \frac{1}{c}\dot{p}\right) = 0 \quad \text{and} \tag{1c}$$

$$p(x, 0) = 0, \qquad \dot{p}(x, 0) = 0, \quad x \in \bar{\Omega}. \tag{1d}$$

In these equations $p$ denotes pressure; $x$ is the position vector, $t$ is time; $\nu$ is the outward unit normal on $\Gamma$; $c$ is the velocity of wave propagation: $\Delta$ is the Laplace operator, and an overdot denotes derivative with respect to time. $p_\nu$ denotes the normal derivative of the pressure $p$, $f_N$ is a prescribed function. Condition (1c), in which $r$ is radial distance and $p_r$ the derivative of the pressure along the radial direction, is the Sommerfeld radiation condition. As indicated by (1d) the system is taken to be initially at rest.

The main difficulty associated with the solution of (1) is the need to ensure that the radiation condition (1c) is satisfied at infinity. To solve this problem using numerical methods based on the spatial discretization of the domain would require that in the limit one consider the complete, unbounded region $\Omega$, a requirement that renders this approach impractical. One way to make this problem manageable is to truncate the exterior region by introducing an artificial boundary $\Gamma_a$ that contains $\Gamma$ in its interior; this gives rise to a bounded subdomain $\Omega_a$, as shown in Fig. 1(b). In order for the solution $p$ to coincide with that of the original problem within the truncated region $\Omega_a$, it is necessary to specify a boundary condition on $\Gamma_a$ that will ensure that the outgoing waves crossing $\Gamma_a$ are undisturbed by the presence of this boundary. This boundary condition, which can be determined in terms of the actual solution $p$ on $\Gamma_a$, as will be shown in the next section, is of the form

$$p_\nu(x, t) = \mathcal{F}[p^t(\cdot, \cdot)](x), \quad x \in \Gamma_a, \tag{2}$$

in which $x$ is position vector, the dots following $p^t$ indicate dummy variables and $\mathcal{F}$ is an integral operator that depends on $p^t$, the time history of $p$, i.e.

$$p^t(t) = p(t - \tau), \quad \forall \tau: \quad 0 \leqslant \tau \leqslant t. \tag{3}$$

## 3. The absorbing boundary

### 3.1. Development

To determine the exact form of the operator $\mathcal{F}$ we consider the following problem associated with the original problem (1). Our procedure is borrowed from [2], which was developed originally for two-dimensional problems. We Laplace-transform (1a) with respect to time to obtain

$$s^2 \hat{p}(x, s) = c^2 \Delta\hat{p}(x, s), \quad x \in \Omega, \tag{4}$$

where $s$ is the Laplace transform variable and a caret over a variable such as $p$ denotes its Laplace transform. Suppose now that the surface $\Gamma_a$ is smooth and convex, and let $\Omega^+$ be the exterior of $\Gamma_a$ ($\Gamma_a$ need not be a sphere) (Fig. 1(b)). We focus on $\hat{p}$ in $\Omega^+$ and formulate the following auxiliary Dirichlet problem in $\Omega^+$ for an auxiliary field $\hat{P}$:

$$s^2\hat{P}(x, s; t) = c^2 \Delta\hat{P}(x, s; t), \quad x \in \Omega^+, \tag{5a}$$

with the boundary condition,

$$\hat{P}(x, s; t) = p(x, t), \quad x \in \Gamma_a. \tag{5b}$$

In (5) the use of a semicolon before $t$ implies that $t$ acts merely as a parameter. Then, by virtue of Duhamel's principle [7], one can show that (Appendix I)

$$\hat{p}(x, s) = \int_0^\infty e^{-st}\hat{P}(x, s; t)\, dt, \quad x \in \bar{\Omega}^+, \tag{6a}$$

and, hence, also

$$\hat{p}_\nu(x, s) = \int_0^\infty e^{-st} \hat{P}_\nu(x, s; t) \, dt \,, \quad x \in \Gamma_a \,. \tag{6b}$$

Eq. (6a) together with Eqs. (5) ensure that the solution $\hat{p}$ in $\Omega^+$ will coincide with the solution $\hat{p}$ in $\Omega$ from (4). From (5b) it can also be seen that the normal derivative $\hat{P}_\nu$ on $\Gamma_a$ will be a linear functional of $p(\cdot, t)$ on $\Gamma_a$. Let us denote this dependency by

$$\hat{P}_\nu(x, s; t) = \hat{\mathscr{F}}[p(\cdot, t)](x, s) \,, \quad x \in \Gamma_a \,, \tag{7a}$$

where $\hat{\mathscr{F}}$ denotes a functional. By substituting (7a) into (6b) there results

$$\hat{p}_\nu(x, s) = \hat{\mathscr{F}}[\hat{p}(\cdot, s)](x, s) \,, \quad x \in \Gamma_a \,. \tag{7b}$$

Then, translation of (7b) back to the time-domain yields

$$p_\nu(x, t) = \mathscr{F}[p'(\cdot, \cdot)](x) \,, \quad x \in \Gamma_a \,. \tag{7c}$$

Hence, in (7c) we recovered the form anticipated in (2); the exact operator $\mathscr{F}$ in (7c) can also be expressed as

$$\mathscr{F}[p'(\cdot, \cdot)](x) = \int_0^t \int_{\Gamma_a} K(|x - y|, t - \zeta) p(y, \zeta) \, dy \, d\zeta \,, \quad x, y \in \Gamma_a \,, \quad t > 0 \,, \tag{8}$$

where the kernel $K$ depends on position and time. Thus, $\mathscr{F}$ denotes a functional of the values of the pressure $p(y, \zeta)$ for $y$ ranging over $\Gamma_a$ and $\zeta$ from 0 to $t$. In other words, $\mathscr{F}$ merely expresses the fact that at any given instant $t$ the motion at every point on the artificial boundary $\Gamma_a$ is coupled with the time histories of all other points on $\Gamma_a$. The nonlocal character of the exact $\mathscr{F}$ makes it unsuitable for implementation in the context of the finite element method. Even if the spatial nonlocality, implied by the surface integral in (8), were relaxed, the temporal nonlocality, implied in (8) by the convolution integral, is particularly cumbersome to implement as it requires the extensive storage of time histories. It is, thus, only natural to seek approximations to the exact $\mathscr{F}$ aiming primarily at reducing the temporal nonlocality. It will be shown that this procedure also reduces automatically the spatial nonlocality. To this end, we turn again to the auxiliary Dirichlet problem defined by (5) and introduce, borrowing from geometrical optics [7], an asymptotic expansion for $\hat{P}$ of the form

$$\hat{P}(x, s; t) \sim e^{-(s/c)\chi(x)} \sum_{k=0}^\infty \left[ \frac{c}{(s + \gamma)a} \right]^k A^{(k)}(x, t) \,, \quad x \in \Omega^+ \,, \tag{9a}$$

where $a$ is a characteristic length of the absorbing boundary (e.g. in the case of a spherical $\Gamma_a$, $a$ is the radius), $\chi(x)$ and $A^{(k)}(x, t)$ are as yet unknown functions, and $\gamma$ is an arbitrary nonnegative parameter which is introduced for stability (discussed in a subsequent section).[1] From a physical point of view, its value controls the amount of numerical damping introduced through the boundary $\Gamma_a$. We require that the functions $\chi(x)$ and $A^{(k)}(x, t)$ satisfy the following conditions on $\Gamma_a$:

$$\chi(x) = 0 \,, \quad A^{(0)}(x, t) = p(x, t) \quad \text{and} \quad A^{(k)}(x, t) = 0 \quad \text{for } k \geqslant 1 \,, \quad x \in \Gamma_a \,. \tag{9b}$$

Eqs. (9) ensure that $\hat{P}$ is outgoing and that (5b) is satisfied automatically for any functions $\chi(x)$ and $A^{(k)}(x, t)$. Eq. (9a), by virtue of (9b), yields for $\hat{P}_\nu$ on $\Gamma_a$

$$\hat{P}_\nu(x, s; t) = -\frac{s}{c} \chi_\nu A^{(0)}(x, t) + \sum_{k=0}^\infty A_\nu^{(k)}(x, t) \left[ \frac{c}{(s + \gamma)a} \right]^k \,, \quad x \in \Gamma_a \,. \tag{10a}$$

Substitution of (10a) in (6b) will therefore yield

---

[1] More generally, one might consider that $\gamma$ varies with $k$ and replace $\gamma$ by $\gamma_k$ in (9a).

$$\hat{p}_\nu(x, s) = -\frac{s}{c}\chi_\nu \hat{A}^{(0)}(x, s) + \sum_{k=0}^{\infty} \hat{A}_\nu^{(k)}(x, s)\left[\frac{c}{(s + \gamma)a}\right]^k, \quad x \in \Gamma_a. \tag{10b}$$

From (10b) and (6b) it can be seen that, once the unknown functions $\chi(x)$ and $A^{(k)}(x, t)$ are determined, an expression for the normal derivative $p_\nu$ on $\Gamma_a$ will be possible by translating (10b) back to the time-domain. To determine $\chi(x)$ and $A^{(k)}(x, t)$, we proceed by introducing (9a) into (5a) and matching the coefficients of the nonnegative powers of $s$ and of the negative powers of the monomials $(s + \gamma)$. There results

$$s^2 \frac{1}{c^2}[|\nabla\chi|^2 - 1]A^{(0)} + s\left\{\frac{1}{ac}[|\nabla\chi|^2 - 1]A^{(1)} - \frac{2}{c}\nabla\chi \cdot \nabla A^{(0)} - \frac{1}{c}\Delta\chi A^{(0)}\right\}$$

$$+ \left\{\frac{1}{c^2}[|\nabla\chi|^2 - 1]\left[-\gamma\frac{c}{a}A^{(1)} + \frac{c^2}{a^2}A^{(2)}\right] - \frac{2}{a}\nabla\chi \cdot \nabla A^{(1)} - \frac{1}{a}\Delta\chi A^{(1)} + \Delta A^{(0)}\right\}$$

$$+ \sum_{k=1}^{\infty} \frac{1}{(s + \gamma)^k}\left\{\frac{1}{c^2}[|\nabla\chi|^2 - 1]\left[\gamma^2\frac{c^k}{a^k}A^{(k)} - 2\gamma\frac{c^{k+1}}{a^{k+1}}A^{(k+1)} + \frac{c^{k+2}}{a^{k+2}}A^{(k+2)}\right]\right.$$

$$- \frac{2}{c}\nabla\chi \cdot \left[-\gamma\frac{c^k}{a^k}\nabla A^{(k)} + \frac{c^{k+1}}{a^{k+1}}\nabla A^{(k+1)}\right]$$

$$\left. - \frac{1}{c}\Delta\chi\left[-\gamma\frac{c^k}{a^k}A^{(k)} + \frac{c^{k+1}}{a^{k+1}}A^{(k+1)}\right] + \frac{c^k}{a^k}\Delta A^{(k)}\right\} = 0. \tag{11}$$

By setting to zero the coefficients of the various powers of $s$ and of the monomials $(s + \gamma)$ in (11) there result the following differential equations for the functions $\chi(x)$ and $A^{(k)}(x, t)$, $(k \geq 0)$ with $x \in \bar{\Omega}^+$:

$$|\nabla\chi|^2 = 1, \tag{12a}$$

$$2\nabla\chi \cdot \nabla A^{(0)} + \Delta\chi A^{(0)} = 0, \tag{12b}$$

$$2\nabla\chi \cdot \nabla A^{(k)} + \Delta\chi A^{(k)} = a\,\Delta A^{(k-1)} + \frac{\gamma a}{c}[2\nabla\chi \cdot \nabla A^{(k-1)} + \Delta\chi\,A^{(k-1)}], \quad k \geq 1. \tag{12c}$$

The differential equations (12a,b) as well as the recursive set (12c) can be used to determine the unknown functions $\chi(x)$ and $A^{(k)}(x, t)$ for any $k$. To this end, we introduce a new coordinate system in $\bar{\Omega}^+$ to aid in subsequent calculations. Let $\Gamma_a$ be described by the parametric representation $X(u, w)$ where $X$ denotes the position vector on $\Gamma_a$ and $u, w$ are the surface parameters. Then, a new coordinate system is introduced in $\bar{\Omega}^+$ by the description

$$R(u, w, \xi) = X(u, w) + \xi\nu(u, w), \quad \xi \geq 0, \tag{13}$$

where $R$ denotes position vector in $\Omega^+$, $\xi$ is a scalar and $\nu$ is the outward normal to $\Gamma_a$ (Fig. 1(b)). Since $\Gamma_a$ is convex and smooth, the new system is global in $\Omega^+$. Notice that for $\xi = 0$, (13) provides the parametric representation of $\Gamma_a$. Using the expressions derived in Appendix B (B1-B6) for the gradient, the Laplacian and the normal derivative in terms of the components of the Euclidean metric tensor $g_{ij}$ of the new coordinate system and their limiting values $h_{ij}$ on $\Gamma_a$ ($h_{ij} = g_{ij}|_{\xi=0}$), the Gaussian $(K)$ and mean $(H)$ curvatures of $\Gamma_a$, along with Eqs. (9b) and (12), one obtains for the normal derivatives of the unknown functions $\chi$, $A^{(0)}$ and $A^{(1)}$

$$\chi_\nu(x) = \chi_\xi(x) = 1, \quad x \in \Gamma_a, \tag{14a}$$

$$A_\nu^{(0)}(x, t) = A_\xi^{(0)}(x, t) = H(x)A^{(0)}(x, t), \quad x \in \Gamma_a, \tag{14b}$$

$$A_\nu^{(1)}(x, t) = A_\xi^{(1)}(x, t) = \frac{a}{2\sqrt{h(x)}}\left\{\left[\frac{1}{\sqrt{h(x)}}(h_{22}(x)A_u^{(0)}(x, t) - h_{12}(x)A_w^{(0)}(x, t))\right]_u\right.$$

$$\left. + \left[\frac{1}{\sqrt{h(x)}}(-h_{12}(x)A_u^{(0)}(x, t) + h_{11}(x)A_w^{(0)}(x, t))\right]_w\right\}$$

$$+ \frac{a}{2}(H^2(x) - K(x))A^{(0)}(x, t), \quad x \in \Gamma_a. \tag{14c}$$

Letter subscripts above denote partial derivatives. Next, by truncating the series in (10b) one can

construct successive approximations to $\hat{p}_\nu$ and, hence, to the functional $\hat{\mathscr{F}}[\hat{p}]$ in (7b). It can, therefore, be shown that by substituting the Laplace transforms of functions (14) into (10b), while taking into account (9b) and (7b), and keeping none, one or two terms from the series in (10b), the first three approximations for $\hat{p}_\nu$ on $\Gamma_a$ are given as

0th order: $\quad \hat{p}_\nu = \hat{\mathscr{F}}_0[\hat{p}] = -\dfrac{s}{c}\,\hat{p}$ , $\qquad\qquad\qquad\qquad\qquad\qquad\qquad\qquad$ (15a)

1st order: $\quad \hat{p}_\nu = \hat{\mathscr{F}}_1[\hat{p}] = -\dfrac{s}{c}\,\hat{p} + H\hat{p}$ , $\qquad\qquad\qquad\qquad\qquad\qquad$ (15b)

2nd order: $\quad \hat{p}_\nu = \hat{\mathscr{F}}_2[\hat{p}] = -\dfrac{s}{c}\,\hat{p} + H\hat{p}$

$$+ \frac{c}{2(s+\gamma)}\left\{\frac{1}{\sqrt{h}}\left[\left(\frac{1}{\sqrt{h}}(h_{22}\hat{p}_u - h_{12}\hat{p}_w)\right)_u + \left(\frac{1}{\sqrt{h}}(-h_{12}\hat{p}_u + h_{11}\hat{p}_w)\right)_w\right]\right.$$

$$\left. + (H^2 - K)\hat{p}\right\} , \qquad\qquad\qquad\qquad\qquad\qquad\qquad\qquad\qquad (15c)$$

where $\hat{\mathscr{F}}_k$ $(k = 0, 1, 2)$ denotes the approximate functional of $k$th order. Translation of (15) back to the time-domain yields

0th order: $\quad p_\nu = -\dfrac{1}{c}\,\dot{p}$ , $\qquad\qquad\qquad\qquad\qquad\qquad\qquad\qquad\qquad$ (16a)

1st order: $\quad p_\nu = -\dfrac{1}{c}\,\dot{p} + Hp$ , $\qquad\qquad\qquad\qquad\qquad\qquad\qquad\qquad$ (16b)

2nd order: $\quad \dot{p}_\nu + \gamma p_\nu = -\dfrac{1}{c}\,\ddot{p} + \left(H - \dfrac{\gamma}{c}\right)\dot{p} + H\gamma p$

$$+ \frac{c}{2}\left\{\frac{1}{\sqrt{h}}\left[\left(\frac{1}{\sqrt{h}}(h_{22}p_u - h_{12}p_w)\right)_u + \left(\frac{1}{\sqrt{h}}(-h_{12}p_u + h_{11}p_w)\right)_w\right]\right.$$

$$\left. + (H^2 - K)p\right\} , \qquad\qquad\qquad\qquad\qquad\qquad\qquad\qquad\qquad (16c)$$

Conditions (16) are the desired approximations of the operator symbol in (2); the first of these is the well-known plane wave approximation (PWA) [29]. We remark that the second-order designation of condition (15c) is prompted by the fact that (15c) agrees with the exact representation up to order $(s + \gamma)^{-1}$; that is, the error is of order $(s + \gamma)^{-2}$. Notice that the lower-order conditions (16a) and (16b) are completely local in space whereas the second-order condition (16c) is only weakly nonlocal due to the presence of second-order tangential derivatives. It is possible to obtain higher-order conditions following the systematic process outlined above; however, as evidenced by (16), higher-order conditions will be characterized by increasing complexity and increasing loss of the local character attained by (16). Indeed, as can be seen from (16c), the temporal locality is affected already; whereas (16a) and (16b) involve only the normal derivative of the pressure $p_\nu$, (16c) introduces the first time derivative of $p_\nu$ as well. The latter calls for a special implementation scheme, which is addressed in a subsequent section.

## 3.2. Special absorbing surfaces

Conditions (16) can be written for various specialized surfaces; here we are interested particularly in ellipsoidal and spherical absorbing boundaries. Our numerical experiments have been performed using a spherical absorbing boundary; however, for numerical applications involving long scatterers, ellipsoidal absorbing surfaces seem best suited as they result, potentially, in smaller computational domains than spherical absorbing surfaces. We use the following surface parameterization for an ellipsoidal absorbing boundary (Fig. 2a):

$$x = a\cos\theta\sin\phi , \qquad\qquad\qquad\qquad\qquad\qquad\qquad\qquad\qquad (17a)$$

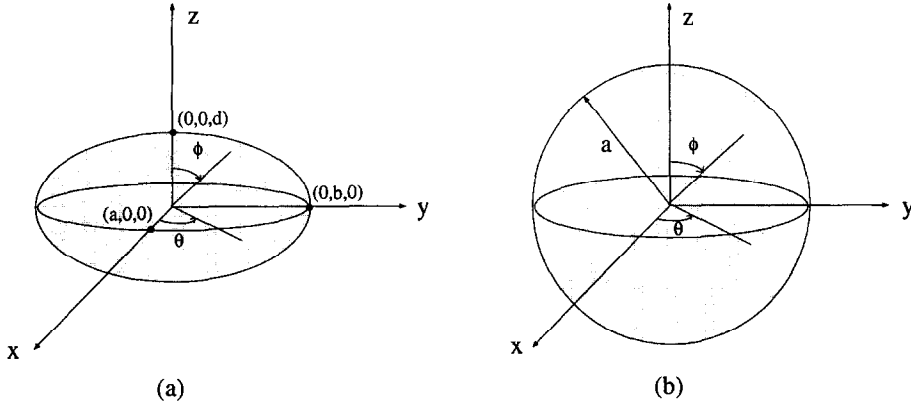$$y = b\sin\theta\sin\phi , \qquad\qquad\qquad\qquad\qquad\qquad\qquad\qquad\qquad (17b)$$

Fig. 2. Geometry of particular absorbing surfaces; (a) ellipsoidal surface; (b) spherical surface.

$$z = d \cos \phi \,, \quad \text{with } \phi \in (0, \pi) \text{ and } \theta \in [0, 2\pi) \,, \tag{17c}$$

where $a$, $b$ and $d$ above are the semiaxes of the ellipsoid along the $x$, $y$ and $z$ axes; $\phi$ denotes the polar angle and $\theta$ the meridional angle (Fig. 2a). It can then be shown that

$$h_{11} = a^2 \cos^2\theta \cos^2\phi + b^2 \sin^2\theta \cos^2\phi + d^2 \sin^2\phi \,, \tag{18a}$$

$$h_{22} = (a^2 \sin^2\theta + b^2 \cos^2\theta) \sin^2\phi \,, \tag{18b}$$

$$h_{12} = (b^2 - a^2) \sin \theta \cos \theta \sin \phi \cos \phi \,, \tag{18c}$$

$$h = [a^2 b^2 \cos^2\phi + d^2 \sin^2\phi (a^2 \sin^2\theta + b^2 \cos^2\theta)] \sin^2\phi \,, \tag{18d}$$

$$K = \frac{a^2 b^2 d^2}{[a^2 b^2 + [d^2(a^2 - b^2) \sin^2\theta - b^2(a^2 - d^2)] \sin^2\phi)]^2} \,, \tag{18e}$$

$$H = -\frac{abd[a^2 + b^2 + [(a^2 - b^2) \sin^2\theta - (a^2 - d^2)] \sin^2\phi]}{2[a^2 b^2 + [d^2(a^2 - b^2) \sin^2\theta - b^2(a^2 - d^2)] \sin^2\phi)]^{3/2}} \,. \tag{18f}$$

With these equations, conditions (16) can be easily written for the ellipsoidal surface after noting that $u \equiv \phi$ and $w \equiv \theta$ in (16c). For the particular case of a spherical absorbing boundary (Fig. 2b), with $a = b = d$, (16) reduce to

$$p_r = -\frac{1}{c} \dot{p} \,, \tag{19a}$$

$$p_r = -\frac{1}{c} \dot{p} - \frac{1}{a} p \,, \tag{19b}$$

$$\dot{p}_r + \gamma p_r = -\frac{1}{c} \ddot{p} - \left(\frac{1}{a} + \frac{\gamma}{c}\right) \dot{p} - \frac{\gamma}{a} p + \frac{c}{2a^2 \sin \phi} \left[ (p_\phi \sin \phi)_\phi + \frac{1}{\sin \phi} p_{\theta\theta} \right] \,. \tag{19c}$$

Notice that for the spherical case the last term in (16c) is identically zero, since $H^2 - K \equiv 0$ for all points on a sphere [19]. We recently [25] used condition (19c) in its axisymmetric form ($p_{\theta\theta} \equiv 0$) in order to solve transient fluid–structure interaction problems using standard finite element techniques.

It is noteworthy that, for the particular case of spherical boundaries, condition (19b) is the same as the first-order condition developed by Bayliss and Turkel [3]. Condition (19c) can also be shown to be identical to the second-order Bayliss and Turkel condition provided one chooses

$$\gamma = \gamma_0 = \frac{c}{a} \,. \tag{20}$$

Jones [20] developed a three-dimensional second-order condition for general convex geometries by extending to three dimensions the two-dimensional condition developed earlier by Kriegsmann et al. [27] using an ad-hoc procedure. Jones's condition coincides with (16c) for $\gamma = 0$; it will be seen, however, that (16c) with $\gamma = 0$ is not, in general, stable for applications in the time-domain.

### 3.3. Stability

Before one can use absorbing boundary conditions such as (16) it is necessary to ensure the well-posedness of the ensuring problem, as the use of asymptotic expansions such as (9a) does not automatically guarantee the stability of the solution. The practical consequence of artificial boundary conditions that lead to ill-posed problems is that the resulting errors usually grow exponentially in time. Here, we study the stability of the absorbing boundary conditions (16) in order to preclude exponential error growth. We start with the spherical conditions (19); we shall further assume that the boundary of the cavity $\Gamma$ (Fig. 1) is also a concentric sphere with radius $a_0$. The procedure used below can be equally applied to the two-dimensional case; the proof herein is based on ideas developed for two-dimensional problems in [17]. To illustrate, we consider a Neumann problem in the unbounded region $\Omega$ $(r > a_0)$ and in the Laplace transformed domain

$$s^2 \hat{p}(x, s) = c^2 \Delta \hat{p}(x, s) , \quad x \in \Omega \ (r > a_0) , \tag{21a}$$

$$\hat{p}_\nu(x, s) = \hat{f}_N , \quad x \in \Gamma \ (r = a_0) . \tag{21b}$$

Next, we introduce a spherical artificial boundary $\Gamma_a$ at $r = a$; we seek to approximate $\hat{p}$ with $\hat{q}$, where $\hat{q}$ satisfies the field equation (21a) in the truncated domain $\Omega_a$ $(a_0 < r < a)$ and the prescribed data (21b). In addition, $\hat{q}_\nu$ satisfies on $\Gamma_a$ $(r = a)$ either of the absorbing boundary conditions (15). Then, the error $\hat{E} = \hat{p} - \hat{q}$ will satisfy

$$s^2 \hat{E}(x, s) = c^2 \Delta \hat{E}(x, s) , \quad x \in \Omega_a \ (a_0 < r < a) , \tag{22a}$$

$$\hat{E}_\nu(x, s) = 0 , \quad x \in \Gamma \ (r = a_0) , \tag{22b}$$

$$\hat{E}_\nu(x, s) - \hat{\mathscr{F}}_k[\hat{E}](x, s) = \hat{\Psi}(x, s) , \quad x \in \Gamma_a \ (r = a) , \quad k = 0, 1, 2 , \tag{22c}$$

where

$$\hat{\Psi}(x, s) = \hat{\mathscr{F}}[\hat{p}\,](x, s) - \hat{\mathscr{F}}_k[\hat{p}\,](x, s) , \quad x \in \Gamma_a \ (r = a) . \tag{22d}$$

For problem (22) above, $\hat{\Psi}$ represents data on $\Gamma_a$. We recall that $\hat{\mathscr{F}}[\hat{p}\,]$ represents the exact boundary condition on $\Gamma_a$; its expression for the specific geometry is known in terms of analytic functions. Hence, from (22d), $\hat{\Psi}$ is known; moreover, it is possible to show that in the non-homogeneous case ($\hat{\Psi} \neq 0$) there are no poles for $\hat{E}$ in the right halfplane of the complex plane. If, furthermore, one can show that problem (22) admits no non-zero solutions for $\Re e\ s \geq 0$ and for zero data $\hat{\Psi}$ ($\hat{\Psi} = 0$), then there will be no solutions for the error $E$ of the form $E = e^{\eta t}$ for positive $\eta$ and, therefore, no exponential error growth since there will be no poles for $E$ in the right halfplane. The solution $q$ corresponding to the approximate boundary conditions will, in general, be bounded and, in transient cases, expected to decay as time increases.

We show, next, that problem (22) has no non-zero solutions for $\Re e\ s \geq 0$ if any of the three functionals $\hat{\mathscr{F}}_k$ ($k = 0, 1, 2$) is used in (22c). We illustrate using $\hat{\mathscr{F}}_2$; the proof for the simpler functionals $\hat{\mathscr{F}}_0$ and $\hat{\mathscr{F}}_1$ is trivial. We recall that the annular domain $\Omega_a$ is spherical; it is thus justifiable to express the solution $\hat{E}(sr, \phi, \theta)$ in series of the tesseral harmonics $P_n^{(m)}(\cos \phi) \cos m\theta$ and $P_n^{(m)}(\cos \phi) \sin m\theta$, where $P_n^{(m)}$ denotes the associated Legendre function of first kind, of degree $n$ and order $m$ (applying Fourier transforms with respect to the two angular coordinates would yield the same result). Therefore

$$\hat{E}(sr, \phi, \theta) = \sum_{n,m} U^{(n)}(sr) P_n^{(m)}(\cos \phi)(a_{nm} \cos m\theta + b_{nm} \sin m\theta) . \tag{23}$$

Then, by virtue of (23), problem (22) gives rise to $(n + 1)$ problems $(n = 0, 1, \ldots, \infty)$ for the radial components $U^{(n)}$ of $\hat{E}$ of the form

$$(r^2 U_r^{(n)})_r - n(n + 1)U^{(n)} = \frac{s^2 r^2}{c^2} U^{(n)}, \quad \text{in } \Omega_a \; (a_0 < r < a), \tag{24a}$$

$$U_r^{(n)} = 0, \quad \text{on } \Gamma \; (r = a_0), \tag{24b}$$

$$U_r^{(n)} = -\left\{ \frac{s}{c} + \frac{1}{a} + \frac{c}{2a^2(s + \gamma)} [n(n + 1)] \right\} U^{(n)}, \quad \text{on } \Gamma_a \; (r = a). \tag{24c}$$

Suppose now that $U^{(n)} \neq 0$; then $\bar{U}^{(n)} \neq 0$, where a bar over $U^{(n)}$ denotes complex conjugate. Let $s = \alpha + i\beta$. Next, multiply (24a) by $\bar{U}^{(n)}$ and integrate over $\Omega_a$. After integrating the resulting expressions by parts and using the divergence theorem, as well as (24b) and (24c), there results:

$$\frac{\alpha^2 - \beta^2}{c^2} \int_{a_0}^{a} |U^{(n)}|^2 r^2 \, dr + \int_{a_0}^{a} |U_r^{(n)}|^2 r^2 \, dr + n(n + 1) \int_{a_0}^{a} |U^{(n)}|^2 \, dr$$

$$+ a^2 \left[ \frac{\alpha}{c} + \frac{1}{a} + \frac{c(\alpha + \gamma)}{2a^2[(\alpha + \gamma)^2 + \beta^2]} n(n + 1) \right] |U^{(n)}(a)|^2 = 0, \tag{25a}$$

$$\frac{2\alpha\beta}{c^2} \int_{a_0}^{a} |U^{(n)}|^2 r^2 \, dr + a^2 \left[ \frac{\beta}{c} - \frac{c\beta}{2a^2[(\alpha + \gamma)^2 + \beta^2]} n(n + 1) \right] |U^{(n)}(a)|^2 = 0. \tag{25b}$$

For $\beta = 0$ and $\alpha \geqslant 0$, (25a) leads to a contradiction since the terms on the left-hand side of (25a) are strictly positive; hence our original supposition $(U^{(n)} \neq 0)$ is false.

For $\beta \neq 0$ and $\alpha \geqslant 0$ (25a) leads to

$$0 \geqslant \frac{\alpha^2 - \beta^2}{c^2} \int_{a_0}^{a} |U^{(n)}|^2 r^2 \, dr + n(n + 1) \int_{a_0}^{a} |U^{(n)}|^2 \, dr$$

$$\geqslant \left[ \frac{\alpha^2 - \beta^2}{c^2} + \frac{n(n + 1)}{a^2} \right] \int_{a_0}^{a} |U^{(n)}|^2 r^2 \, dr, \tag{26a}$$

and finally to

$$\beta^2 \geqslant \frac{n(n + 1)c^2}{a^2}. \tag{26b}$$

Then, Eq. (25b), by virtue of (26b), yields

$$0 \geqslant \frac{1}{c} - \frac{c}{2a^2[(\alpha + \gamma)^2 + \beta^2]} n(n + 1) \geqslant \frac{1}{c} - \frac{1}{2c} = \frac{1}{2c} > 0. \tag{27}$$

We have reached again a contradiction; our original supposition is false and, thus, for all $s$ for which $\Re s \geqslant 0$, $U$ is identically zero. We have, thus, shown that conditions (16) are unconditionally stable, with the proviso of spherical boundaries.

The study of the stability of higher-order functionals and/or of lower-order functionals (e.g. second-order) defined over arbitrary (convex) boundaries is considerably more involved than the preceding simple proof; a complete discussion is beyond the scope of the present paper. We remark, however, that in [2], Barry et al. introduced the concept of dissipativity as a criterion for ensuring that the errors remain bounded and gave two sufficient (but not necessary) conditions for the dissipativity of the operators in the two-dimensional case for general convex geometries. By extending their arguments to three dimensions, one can show that the following inequality must be satisfied for the stability parameter $\gamma$ [24]:

$$\gamma \geqslant \gamma_{cr} = \frac{c}{2} \left( -\frac{H^2 - K}{H} \right)_{max} \tag{28}$$

In this equation the subscript max denotes an upper bound for the positive quantity $-(H^2 - K)/H$. The role of $\gamma$ in (16) should now be clear; $\gamma$ is a positive constant introduced in order to ensure the stability of the absorbing boundary conditions and should be greater than or equal to a critical value $\gamma_{cr}$. For the particular case of a spherical absorbing boundary $\gamma_{cr} = 0$ since $H^2 - K \equiv 0$ for all points on a sphere [19].

For most of the applications considered herein, we used spherical absorbing boundaries with $\gamma = \gamma_0$ (see (20)), which satisfies the stability inequality (28); we justify the use of the particular value for $\gamma$ in the numerical results section. However, as we argue in the same section, it is possible to identify an optimal value for $\gamma$ that can be shown to yield minimal errors; since such a value is frequency dependent, it can be used to advantage only when one is interested in frequency-domain, and not in time-domain, computations.

## 4. Finite element discretization

In order to discretize the problem within $\Omega_a$ using finite elements, we return to the strong statement (1), in order to recast it into a weak form. Notice, that the infinite domain $\Omega$ in (1) will now be replaced by the finite annular region $\Omega_a$. To construct the corresponding weak form we first multiply (1a) by a test function $\delta p$ not subject to any boundary condition on $\Gamma$ or $\Gamma_a$, integrate the result over $\Omega_a$, and apply the divergence theorem to the test that contains the Laplacian operator. We then subtract the integral over $\Gamma$ of (1b) multiplied by the restriction of $\delta p$ to $\Gamma$. This process results in

$$\frac{1}{c^2} \int_{\Omega_a} \delta p \ddot{p} \, d\Omega_a + \int_{\Omega_a} \nabla \delta p \cdot \nabla p \, d\Omega_a - \int_{\Gamma_a} \delta p p_\nu \, d\Gamma_a = -\int_\Gamma f_N \, \delta p \, d\Gamma \, , \tag{29}$$

Replacing $p_\nu$ in the third integral in (29) by conditions (16a) or (16b) is trivial; on the other hand, the higher-order condition (16c), while expected to yield improved accuracy and computational economy due to the need for a smaller buffer region ($\Omega_a$), cannot be readily implemented since it involves both the normal derivative of the pressure $p_\nu$ and its first time derivative $\dot{p}_\nu$. Our aim is to make the condition amenable to standard integration techniques typically used for interior problems. We show that this can be achieved through the introduction of additional degrees of freedom on the artificial boundary, similarly to our earlier work in two dimensions [21–25].

### 4.1. Decomposition

Let $q^{(1)}$ and $q^{(2)}$ denote auxiliary variables on $\Gamma_a$. Then, one can show via Laplace transforms in time that the following set of three equations is equivalent to (16c)

$$-p_\nu = \frac{1}{c} \dot{p} - Hp - \frac{c}{2\gamma} \mathcal{T} q^{(1)} - \frac{c}{2\gamma} (H^2 - K) q^{(2)} \, , \tag{30a}$$

$$\mathcal{T} p - \mathcal{T} q^{(1)} - \frac{1}{\gamma} \mathcal{T} \dot{q}^{(1)} = 0 \, , \tag{30b}$$

$$p - q^{(2)} - \frac{1}{\gamma} \dot{q}^{(2)} = 0 \, . \tag{30c}$$

Here, $\mathcal{T}$ is the differential operator defined by

$$\mathcal{T} \cdot = \frac{1}{\sqrt{h}} \left\{ \left[ \frac{1}{\sqrt{h}} (h_{22}(\cdot)_u - h_{12}(\cdot)_w) \right]_u + \left[ \frac{1}{\sqrt{h}} (-h_{12}(\cdot)_u + h_{11}(\cdot)_w) \right]_w \right\} \, . \tag{31}$$

Now multiply (30a) by $\delta p$, (30b) by $\delta q^{(1)}$ and (30c) by $\delta q^{(2)}$, where $\delta q^{(1)}$ and $\delta q^{(2)}$ are appropriate test functions and integrate by parts the terms associated with the operator $\mathcal{T}$. There results

$$-\int_{\Gamma_a} \delta p p_{,\nu} \, d\Gamma_a = \frac{1}{c} \int_{\Gamma_a} \delta p \dot{p} \, d\Gamma_a - \int_{\Gamma_a} H \delta p p \, d\Gamma_a + \frac{c}{2\gamma} \int_{\Gamma_a} \nabla^s \, \delta p \cdot \nabla^s q^{(1)} \, d\Gamma_a$$

$$-\frac{c}{2\gamma} \int_{\Gamma_a} (H^2 - K) \, \delta p q^{(2)} \, d\Gamma_a \,, \tag{32a}$$

$$\frac{c}{2\gamma} \int_{\Gamma_a} \nabla^s \, \delta q^{(1)} \cdot \nabla^s p \, d\Gamma_a - \frac{c}{2\gamma} \int_{\Gamma_a} \nabla^s \, \delta q^{(1)} \cdot \nabla^s q^{(1)} \, d\Gamma_a - \frac{c}{2\gamma^2} \int_{\Gamma_a} \nabla^s \, \delta q^{(1)} \cdot \nabla^s \dot{q}^{(1)} \, d\Gamma_a = 0 \,, \tag{32b}$$

$$-\frac{c}{2\gamma} \int_{\Gamma_a} (H^2 - K) \, \delta q^{(2)} p \, d\Gamma_a + \frac{c}{2\gamma} \int_{\Gamma_a} (H^2 - K) \, \delta q^{(2)} q^{(2)} \, d\Gamma_a + \frac{c}{2\gamma^2} \int_{\Gamma_a} (H^2 - K) \, \delta q^{(2)} \dot{q}^{(2)} \, d\Gamma_a = 0 \,, \tag{32c}$$

in which $\nabla^s$ is the surface gradient (see B7). In addition, $q^{(1)}$, $q^{(2)}$, $\dot{q}^{(1)}$ and $\dot{q}^{(2)}$ are required to vanish at $t = 0$.

Eqs. (32) can then be used to complete the weak-form formulation. The right side of (32a) replaces the third term in (29), and (32b) and (32c) are added to the resultant functional.

It is important to observe that with the replacement for (16c) of (32), (29) will lead, upon spatial discretization, to a symmetric system of ordinary differential equations. In other words, the contributions from the absorbing boundary maintain both the symmetric structure of the interior problem and the sparsity of the associated system matrices.

## 4.2. System matrices

Standard finite element piecewise polynomial approximations are used for approximating the geometry and for the spatial discretization of the pressure $p$ in $\Omega_a$ and on $\Gamma_a$ and of the auxiliary pressures $q^{(1)}$ and $q^{(2)}$ on $\Gamma_a$. The same approximations are used for the functions $p$, $q^{(1)}$ and $q^{(2)}$, as well as their respective weighting functions. Notice that the presence of first-order derivatives in (32) increases the usual smoothness requirements on the artificial boundary; in short, we seek $p$ and $\delta p$ that belong to $H^1(\Omega_a) \times H^1(\Gamma_a)$ where $H^1$ denotes the Sobolev space of degree 1. Similarly, $q^{(1)}$ and $\delta q^{(1)}$ need also belong to $H^1(\Gamma_a)$. Artificial boundary conditions of order higher than the second (not treated herein) might impose even higher smoothness requirements than $H^1(\Gamma_a)$ on $\Gamma_a$; notice, however, that these requirements are local to $\Gamma_a$. We introduce

$$p(x, t) = \psi_1^T(x) p(t) \,, \qquad \delta p(x) = \delta p^T \psi_1(x) \,, \tag{33a}$$

$$q^{(1)}(x, t) = \psi_2^T(x) q^{(1)}(t) \,, \qquad \delta q^{(1)}(x) = \delta q^{(1)T} \psi_2(x) \,, \tag{33b}$$

$$q^{(2)}(x, t) = \psi_3^T(x) q^{(2)}(t) \,, \qquad \delta q^{(2)}(x) = \delta q^{(2)T} \psi_3(x) \,, \tag{33c}$$

in which, $\psi_1$, $\psi_2$ and $\psi_3$ are vectors of shape functions and $p$, $q^{(1)}$ and $q^{(2)}$ are vector fields of the unknown nodal functions in time. Substitution of (33) into (29) and (32) results in a system of ordinary differential equations with the following structure:

$$M\ddot{P} + C\dot{P} + KP = F \,, \tag{34}$$

where $P^T = [p_\Gamma^T, p_{\Omega_a}^T, p_{\Gamma_a}^T, q^{(1)T}, q^{(2)T}]$ and $p_\Gamma$, $p_{\Omega_a}$, $p_{\Gamma_a}$ denote partitions of $p$ over $\Gamma$, $\Omega_a$, and $\Gamma_a$, respectively; $M$, $C$ and $K$ are the mass, damping and stiffness matrices of the system, and $F$ denotes the excitation.

The matrices $M$, $C$ and $K$ have the following form:

$$M = \begin{bmatrix} M^f_{p_\Gamma p_\Gamma} & M^f_{p_\Gamma p_{\Omega_a}} & 0 & 0 & 0 \\ M^f_{p_{\Omega_a} p_\Gamma} & M^f_{p_{\Omega_a} p_{\Omega_a}} & M^f_{p_{\Omega_a} p_{\Gamma_a}} & 0 & 0 \\ 0 & M^f_{p_{\Gamma_a} p_{\Omega_a}} & M^f_{p_{\Gamma_a} p_{\Gamma_a}} & 0 & 0 \\ 0 & 0 & 0 & 0 & 0 \\ 0 & 0 & 0 & 0 & 0 \end{bmatrix} \tag{35a}$$

$$
C = \begin{bmatrix} 0 & 0 & 0 & 0 & 0 \\ 0 & 0 & 0 & 0 & 0 \\ 0 & 0 & C^a_{p_{\Gamma_a}p_{\Gamma_a}} & 0 & 0 \\ 0 & 0 & 0 & C^a_{q^{(1)}q^{(1)}} & 0 \\ 0 & 0 & 0 & 0 & C^a_{q^{(2)}q^{(2)}} \end{bmatrix} ,
$$

(35b)

$$
K = \begin{bmatrix} K^f_{p_\Gamma p_\Gamma} & K^f_{p_\Gamma p_{\Omega_a}} & 0 & 0 & 0 \\ K^f_{p_{\Omega_a}p_\Gamma} & K^f_{p_{\Omega_a}p_{\Omega_a}} & K^f_{p_{\Omega_a}p_{\Gamma_a}} & 0 & 0 \\ 0 & K^f_{p_{\Gamma_a}p_{\Omega_a}} & K^f_{p_{\Gamma_a}p_{\Gamma_a}} + K^a_{p_{\Gamma_a}p_{\Gamma_a}} & K^a_{p_{\Gamma_a}q^{(1)}} & K^a_{p_{\Gamma_a}q^{(2)}} \\ 0 & 0 & K^a_{q^{(1)}p_{\Gamma_a}} & K^a_{q^{(1)}q^{(1)}} & 0 \\ 0 & 0 & K^a_{q^{(2)}p_{\Gamma_a}} & 0 & K^a_{q^{(2)}q^{(2)}} \end{bmatrix} .
$$

(35c)

$M$ and $K$ consist of two sets of block-diagonal matrices; the individual matrices within each block are designated by the superscripts $f$, or $a$, to indicate explicitly that they correspond to the fluid (f), or the absorbing boundary (a). Thus, the top left blocks are the standard mass and stiffness matrices associated with the fluid, and the bottom right blocks in (35b) and (35c) represent, respectively, the effective damping and stiffness introduced by the absorbing boundary. Notice that there is no inertia associated with our approximate absorbing boundary. Also, the only damping in the system comes from the absorbing boundary which is associated with the radiated energy in the actual unbounded system.

Finally, the forcing vector $F$ in (34) is given as

$$
F^T = [F^T_N, 0^T, 0^T, 0^T, 0^T] , \quad \text{with} \quad F_N = -\int_\Gamma f_N \psi_1 \, d\Gamma .
$$

(36)

### 4.3. Impedance-infinite element-local matrices

Since $C^a$ and $K^a$ in (35b,c) are local and symmetric, they can be constructed element by element and incorporated into the equations of motion by standard assembly techniques using existing finite element software. All that is necessary is to incorporate the corresponding element matrices $c^a$ and $k^a$ into the finite element library of an existing software package for interior problems. Then, the same finite element software package can be used to solve the complete system of Eq. (34), in either assembled form, node-by-node, or element-by-element, by means of its own step-by-step time integrator. The element stiffness matrix $k^a$ and the element damping matrix $c^a$ are given as:

$$
k^a = \frac{c}{2\gamma} \begin{bmatrix} \frac{2\gamma}{c} k_{11} & k_{12} & -k_{13} \\ k_{12}^T & -k_{22} & 0 \\ -k_{13}^T & 0 & k_{33} \end{bmatrix} , \quad c^a = \frac{c}{2\gamma^2} \begin{bmatrix} \frac{2\gamma^2}{c^2} c_{11} & 0 & 0 \\ 0 & -c_{22} & 0 \\ 0 & 0 & c_{33} \end{bmatrix} ,
$$

(37a)

with the following definitions for the individual matrices:

$$
k_{11} = -\int_{\Gamma_a^e} H \psi_1 \psi_1^T \, d\Gamma_a^e , \quad k_{22} = \int_{\Gamma_a^e} \bar\nabla^s \psi_2 \cdot \bar\nabla^s \psi_2^T \, d\Gamma_a^e , \quad k_{33} = \int_{\Gamma_a^e} (H^2 - K) \psi_3 \psi_3^T \, d\Gamma_a^e ,
$$

$$
k_{12} = \int_{\Gamma_a^e} \bar\nabla^s \psi_1 \cdot \bar\nabla^s \psi_2^T \, d\Gamma_a^e , \quad k_{13} = \int_{\Gamma_a^e} (H^2 - K) \psi_1 \psi_3^T \, d\Gamma_a^e ,
$$

$$
c_{11} = \int_{\Gamma_a^e} \psi_1 \psi_1^T \, d\Gamma_a^e , \quad c_{22} = k_{22} , \quad c_{33} = k_{33} ,
$$

(37b)

where $d\Gamma_a^e$ and the operator $\bar\nabla^s$ denote the area differential and the approximation of the surface gradient $\nabla^s$ on an element $\Gamma_a^e$ of $\Gamma_a$, respectively. We remark that the kernels of the integrals in (32a)

and (32b) that involve the surface gradient $\nabla^s$ may, in the continuous case, become singular depending on the choice of surface parameterization. For example, if a spherical coordinate system is used (Fig. 2b), then the kernels will be singular at the poles, i.e. $\phi = 0$ or $\pi$. However, for the discrete approximation, the resulting kernels will be non-singular and readily integrable if one uses local cartesian coordinate systems.

The element matrices (37a) essentially give rise to a new finite element which is capable of absorbing the waves that reach the artificial boundary while simulating the effect of the truncated infinite domain; thence the impedance-infinite element designation.

We further remark that the element defined by (37) is a surface-only element (Fig. 3); one need only mesh the finite region $\Omega_a$ and simply attach the impedance-infinite element on the boundary $\Gamma_a$ without any further discretization within the infinite exterior region. To illustrate, let us assume that linear isoparametric approximations $N$ are used and that $\psi_1 = \psi_2 = \psi_3 = N$. Then all that is needed in order to describe the impedance-infinite element are four nodes on the boundary $\Gamma_a$ with three degrees of freedom per node (Fig. 3), as it can be readily inferred from (37); the impedance-infinite element will be completely defined by the pair of symmetric $(12 \times 12)$ damping and stiffness matrices. Notice further that, in the case of a spherical absorbing boundary, the quantity $H^2 - K$ vanishes identically and hence the submatrices $k_{13}$ and $k_{33}$ in (37) are identically zero; in that case, only two degrees of freedom per node are needed to describe the impedance-infinite element, effectively reducing the dimensions of the resulting matrices to $(8 \times 8)$.

In order to complete our description, we remark that in (33) we approximated $q^{(1)}$ directly. Notice, however, that $q^{(1)}$ does not explicitly appear in (32); instead only its derivatives $\nabla^s q^{(1)}$ are present. Therefore, any approximate solution for $q^{(1)}$ that differs by a constant from the exact solution to $q^{(1)}$ will still satisfy (32). It is evident that the resulting global stiffness and damping matrices, if left untreated, will be rank deficient by one and will therefore lead to unstable solutions. One remedy to the problem, which was successfully used in two-dimensional cases [21–23], is to approximate directly the derivatives of $q^{(1)}$ in place of $q^{(1)}$ itself; this would eliminate the rank deficiency of the global system matrices. In the three-dimensional case, however, this approach lead to poor results at nodes near the singularity points of the parametric representation of the boundary, e.g. close to the poles of a spherical absorbing boundary. An alternative approach to render the system non-singular is to set to zero at one node of a single element on the absorbing boundary the degree of freedom corresponding to $q^{(1)}$. This is the approach we follow here.

The resulting system of Eq. (34) can be solved by standard step-by-step integration schemes. We stress that the present impedance-infinite element, unlike other infinite elements [4,5], can be used equally well in the time- or frequency-domains, since the associated element stiffness and damping matrices are frequency independent. Indeed, in the case of a time-harmonic steady-state excitation $F = \bar{F} e^{i\omega t}$, (34) yields the usual system of algebraic equations:

$$(-\omega^2 M + i\omega C + K)\bar{U} = \bar{F} , \tag{38}$$

which results from seeking a solution of the form $U = \bar{U} e^{i\omega t}$.

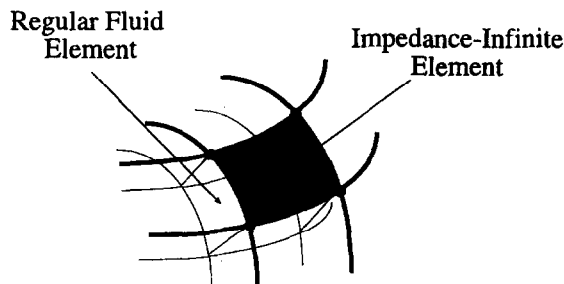Regular Fluid
Element

Impedance-Infinite
Element

Fig. 3. Typical geometry of impedance-infinite element.

## 5. Numerical examples

This section describes numerical experiments conducted in order to assess the performance of the approximate absorbing boundary conditions and of the proposed impedance-infinite element. In our numerical work, we have, thus far, implemented only the spherical conditions (19) and hence, perforce, the discussion will be limited to these. The section is divided into two parts: first, under the heading of exact analysis, we describe the relative performance of the various conditions (19a)–(19c) based on an exact harmonic analysis of a simple Neumann problem in the frequency-domain. These studies allow for the comparison of conditions (19a)–(19c) without the contamination of discretization errors; they also assist in developing rules for the closest required position of the impedance-infinite element in order to ensure satisfactory performance. We also study the role of the stability parameter $\gamma$ in the performance of the second-order condition (19c). Subsequently, under the heading of finite element analysis, we present results in both the frequency- and time-domain obtained by the proposed impedance-infinite element in conjunction with standard finite element techniques.

### 5.1. Exact analysis

Consider a radiation problem from a spherical cavity, as depicted in Fig. 4. $R_i$ denotes the (inner) radius of the cavity $\Gamma$, and $R_o$ the (outer) radius of the concentric spherical absorbing boundary $\Gamma_a$; let the exterior infinite region $\Omega_a \cup \Omega^+$ $(r \geqslant R_i)$ be occupied by a linear, inviscid and compressible fluid characterized by density $\rho$ and speed of sound $c$. Using the spherical coordinate system $(r, \phi, \theta)$ shown in Fig. 4, we seek to solve

$$\Delta p = \frac{1}{c^2} \ddot{p} , \quad \text{in } \Omega_a \cup \Omega^+ , \tag{39a}$$

subject to the Sommerfeld radiation condition (1d) at infinity and a prescribed radial acceleration field on the inner boundary of the cavity of the form

$$p_r = \rho A_0 P_n^{(m)}(\cos \phi) \cos m\theta \, e^{i\omega t} , \quad \text{at } r = R_i , \tag{39b}$$

where $A_0$ is the amplitude of the prescribed field and $P_n^{(m)}$ is the associated Legendre function of the first kind, degree $n$ and order $m$. It can be shown that the exact solution of (39) is given by

$$p = \rho A_0 R_i Q_{ex}(r/R_i, kR_i, n) P_n^{(m)}(\cos \phi) \cos m\theta , \tag{40}$$

in which $Q_{ex}$ represents the radial component of $p$ with frequency measured through the wave number $k = \omega/c$. The explicit formula for $Q_{ex}$ is given in Appendix C. One can also get exact formulas for the radial component of the pressure for the sequence of the approximate problems defined over the
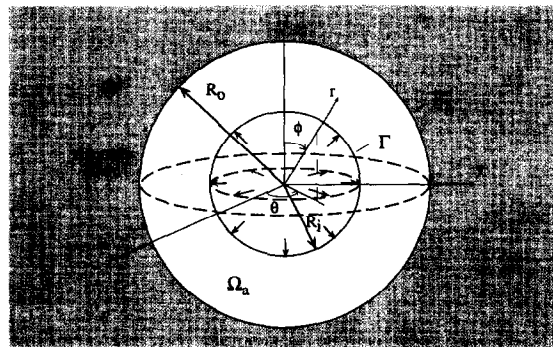


Fig. 4. Model for studying radiation from a spherical cavity.

annular region $\Omega_a$, corresponding to the various approximations (19) of the exact boundary condition on $\Gamma_a$. Analogously to (40) we write

$$p_{app} = \rho A_0 R_i Q^{(j)}_{app}(r/R_i, R_o/R_i, kR_i, n)P^{(m)}_n(\cos \phi) \cos m\theta \ , \tag{41}$$

in which $Q^{(j)}_{app}$ denotes the radial component of the exact solution to the corresponding approximate problem. The superscript $j$ refers to the order of the approximation in accordance with (16) ($j = 0, 1, 2$). The explicit formulas for $Q^{(j)}_{app}$ are given in Appendix C.

From $Q_{ex}$ and $Q^{(j)}_{app}$ one can examine the behavior of the radial component of the exact pressure in the fluid and assess the accuracy of the various approximate absorbing boundary conditions by comparing directly $Q_{ex}$ with the sequence of approximate radial components $Q^{(j)}_{app}$.

From the expressions for $Q_{ex}$ in Appendix C it can be readily verified that its amplitude decreases with increasing frequency $k$, and even more rapidly with increasing distance $r$. Furthermore, for a fixed frequency, the amplitude of $Q_{ex}$ at a given point in the infinite domain decreases with increasing mode $n$ beyond a certain value of $n$. These observations, which are central to the subsequent interpretation of the performance of the various absorbing boundaries, can be deduced from Fig. 5, which depicts the normalized amplitude of $Q_{ex}$ as a function of the normalized distance $(r - R_i)/\lambda$ ($\lambda$ denotes the acoustic wavelength, i.e. $\lambda = 2\pi/k$). Now, let $E$ be the relative error defined by

$$E = \frac{|Q_{ex} - Q^{(j)}_{app}|}{|Q_{ex}|}, \quad \text{for } j = 0, 1, 2 \ . \tag{42}$$

Notice that for $j = 0$ and $j = 1$ the error $E$ depends on $r$, $k$ and on the radial harmonic $n$; for $j = 2$, $E$ depends, in addition, on the value of the stability parameter $\gamma$. It is of interest to seek the optimum value $\gamma_{opt}$ of $\gamma$ that minimizes the error $E$ for a fixed $n$ and for all $r$. One can show that [24]

$$\lim_{(R_o-R_i)/\lambda \to 0} \gamma_{opt} = \frac{n + 1}{2} \frac{c}{R_o} \ , \quad \forall n \geqslant 0 \ . \tag{43}$$

Fig. 6 shows the variation of the optimal values $\gamma_{opt}$ (normalized by $\gamma_0 = c/R_o$) as a function of the normalized position of the absorbing boundary, $(R_o - R_i)/\lambda$. For large values of the abscissa, $\gamma_{opt}$ tends to a constant equal to $\gamma_0$; this is the Bayliss and Turkel [3] value (see Eq. (20)). Notice, that the rapid convergence to this limit, observed for small values of $n$, decreases as $n$ increases. It can also be seen that for the range of harmonics considered ($n$ up to 7), a constant value of $\gamma = \gamma_0$ will be near-optimal,
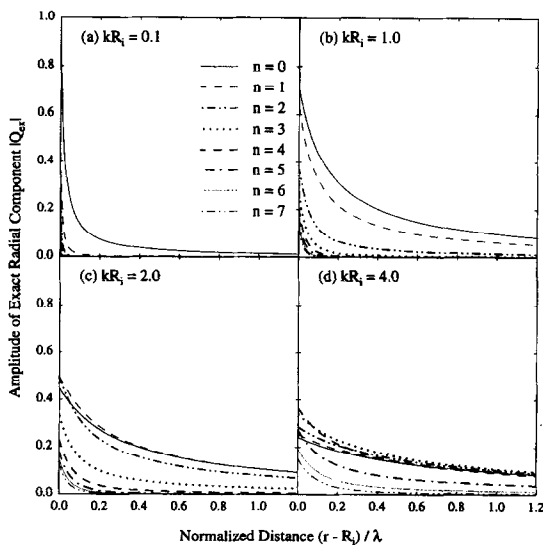


Fig. 5. Exact steady-state response due to harmonic excitation; various frequencies.
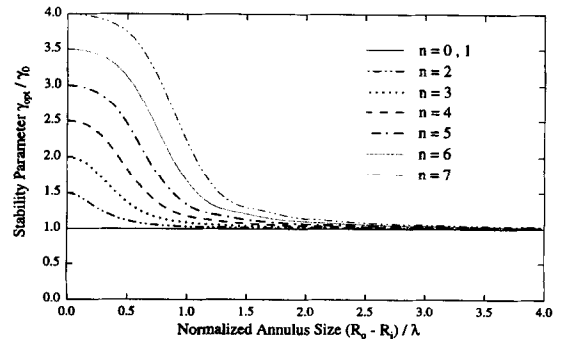
Fig. 6. Optimum values for stability parameter $\gamma$.

provided the absorbing boundary (or the impedance-infinite element) is placed at approximately 1.5 to 2 acoustic wavelengths from the radiator. One can also expect that if the constant value of $\gamma = \gamma_0$ is used at small frequencies and/or distances, the errors will increase the increasing $n$; however, if the dominant modes of an arbitrary excitation signal are within the first few $(n \leqslant 4)$ then placing the absorbing boundary at a distance which is only a fraction of the dominant acoustic wavelength should be expected to yield satisfactory results.

It can also be seen from Fig. 6 that for $n = 0$ and $n = 1$, $\gamma_{opt}$ is identical to $\gamma_0$; it can be further shown that for these values of $n$ the associated error is identically zero. Hence, the second-order condition (19c) with $\gamma = \gamma_0$ is exact for the first two harmonics $n = 0$ and $n = 1$.

It is of interest to examine the behavior of the error function $E$ for different frequencies of excitation, modes $n$, and locations of the various absorbing boundaries. We do so by means of a numerical parametric study. For the limiting zero frequency (long time) condition, however, it is possible to obtain explicit formulas for the corresponding limiting value $E_0$ of $E$. These formulas are given in Table 1 in Appendix D. (Since for the particular value $\gamma = \gamma_{opt}$, (19c) yields the exact limiting solution, i.e., $E_0 = 0$, this case is not listed in the table.) The table also shows the limit of $E_0$ on the absorbing boundary $(r = R_o)$ as the outer radius $R_o$ tends to infinity. For $n > 1$ this error is significant for all the approximate boundary conditions (19). This suggests that none of them may be suitable for static or nearly static problems if the effect of the higher harmonics is significant.

To illustrate how the relative error $E$ varies with the location of the absorbing boundary for various modes $n$, Figs. 7 and 8 depict $E$ versus $R_o/R_i$ for the first six modes $(n = 1 \cdots 6)$, and for frequencies of excitation $kR_i$, a low value of 0.05 (Fig. 7) and a higher one of 0.5 (Fig. 8), corresponding to the various boundary conditions (19). Results for $n = 0$ are not included since all conditions, except for the zeroth-order (19a), are exact. In general, the errors decrease with the order of the approximation; that is, for a fixed frequency and position of the absorbing boundary, the second-order condition (19c) with $\gamma = \gamma_{opt}$ behaves best (solid line), followed by (19c) with $\gamma = \gamma_0$, the first-order (19b) and the zeroth-order (19a). Conversely, for a given tolerance, the use of the second-order (19c) requires a smaller buffer zone. As an example consider the case $kR_i = 0.5$, $n = 2$, and a desirable error of less than 5 percent. According to Fig. 8, the second-order absorbing boundary with $\gamma = \gamma_0$ need be placed at $0.4R_i$ from the radiator, whereas the corresponding distances for the first- and zeroth-order ones are

Table 1
Limiting behavior of relative error $E$ as $k \to 0$; limit as $R_o \to \infty$

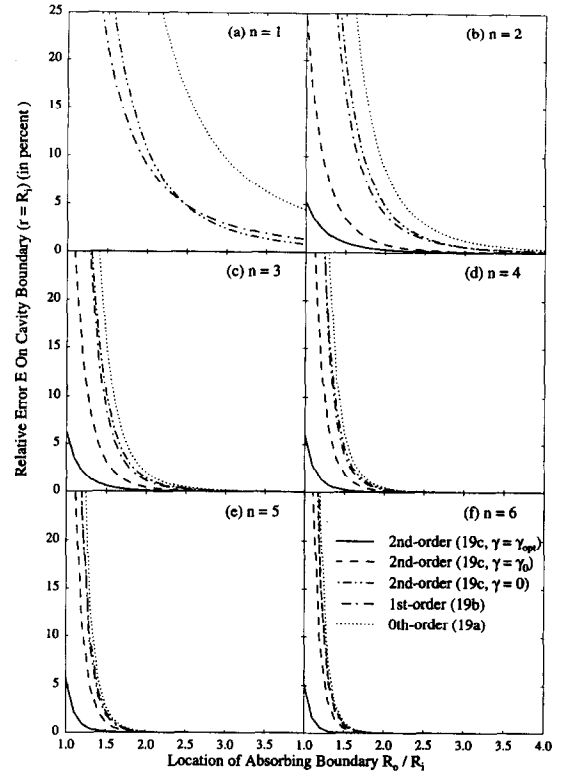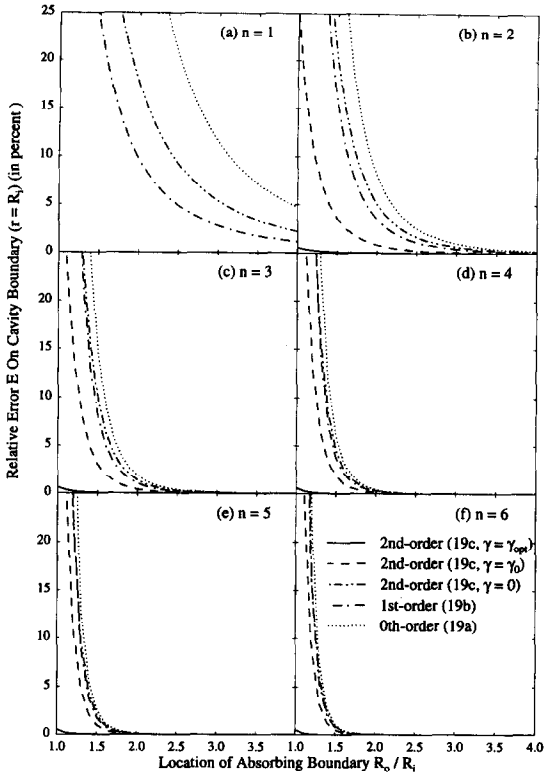| Condition type | $E_0 = \lim_{k \to 0} E \ (n > 0)$ | $\lim_{R_o \to \infty} E_0\vert_{R_o}$ |
|---|---|---|
| (19a) | $\left\| \dfrac{n\left(\dfrac{R_i}{R_o}\right)^n + (n+1)\left(\dfrac{r}{R_o}\right)^n \left(\dfrac{r}{R_i}\right)^{n+1}}{n\left(\dfrac{R_o}{R_i}\right)^{n+1} - n\left(\dfrac{R_i}{R_o}\right)^n} \right\|$ | $\dfrac{n+1}{n}$ |
| (19c) ($\gamma = 0$) | $\left\| \dfrac{n\left(\dfrac{R_i}{R_o}\right)^n + (n+1)\left(\dfrac{r}{R_o}\right)^n \left(\dfrac{r}{R_i}\right)^{n+1}}{(n+1)\left(\dfrac{R_o}{R_i}\right)^{n+1} + n\left(\dfrac{R_i}{R_o}\right)^n} \right\|$ | $1$ |
| (19b) | $\left\| \dfrac{n^2\left(\dfrac{R_i}{R_o}\right)^n + n(n+1)\left(\dfrac{r}{R_o}\right)^n \left(\dfrac{r}{R_i}\right)^{n+1}}{(n+1)^2\left(\dfrac{R_o}{R_i}\right)^{n+1} - n^2\left(\dfrac{R_i}{R_o}\right)^n} \right\|$ | $\dfrac{n}{n+1}$ |
| (19c) ($\gamma = \gamma_0$) | $\left\| \dfrac{n^2(n-1)\left(\dfrac{R_i}{R_o}\right)^n + n(n^2-1)\left(\dfrac{r}{R_o}\right)^n \left(\dfrac{r}{R_i}\right)^{n+1}}{(n+1)^2(n+2)\left(\dfrac{R_o}{R_i}\right)^{n+1} + n^2(n-1)\left(\dfrac{R_i}{R_o}\right)^n} \right\|$ | $\dfrac{n(n^2-1)}{(n+1)^2(n+2)}$ |

Fig. 7. Relative error on the cavity boundary as a function of the location of the absorbing boundary $R_o/R_i$; $kR_i = 0.05$; various harmonics; various absorbing conditions.

Fig. 8. Relative error on the cavity boundary as a function of the location of the absorbing boundary $R_o/R_i$; $kR_i = 0.5$; various harmonics; various absorbing conditions.

$0.9R_i$ and $1.3R_i$, respectively. These differences are more dramatic for the case $n = 1$; for the same tolerance, the zeroth-order requires $R_o > 3.9R_i$, the first-order $R_o > 2.5R_i$, whereas the second-order condition is exact. The differences decrease at higher frequencies but become more pronounced at lower ones. From Figs. 7 and 8 it can also be seen that for a given boundary condition, $E_0$ decreases with increasing frequency; the accuracy increases with the distance $R_o/R_i$ and the rate of decay depends strongly on the mode $n$; using $\gamma = \gamma_{opt}$ instead of $\gamma_0$ improves significantly the performance of the second-order condition when it is placed near the cavity (the improvement is greatest for the lower frequency of excitation); however, whereas $\gamma_{opt}$ can be used to advantage in frequency-domain analyses and in time-domain calculations based on the FFT, it would, unfortunately, not be as practical for direct calculations in the time-domain, since its frequency dependence would introduce convolutions into (19c).

To further examine the sensitivity of the second-order condition (19c) to the frequency of excitation, Fig. 9 depicts the relative error $E$ for the second-order condition (19c) with $\gamma = \gamma_0$, at both the cavity and absorbing boundaries versus $kR_i$ for several modes $n$ and positions of the absorbing boundary $\Gamma_a$. One key observation is that the errors become very small at high frequencies, even if $\Gamma_a$ coincides with the cavity boundary $\Gamma$ (Fig. 9a). This is to be expected since the present approach is based on the high-frequency expansion (9a) borrowed from geometrical optics. At lower frequencies the error on the cavity boundary $\Gamma$ increases significantly, requiring that $\Gamma_a$ be moved some distance away from $\Gamma$. While the errors on $\Gamma_a$ decrease as the distance between these two boundaries increases, they remain significant even at $R_o/R_i = 2$. Fortunately, the effect of these errors on the inner boundary is negligible since the amplitude of the actual response for the higher modes decreases rapidly with distance, as discussed earlier in connection with Fig. 5. It is noteworthy that the errors on the cavity boundary peak around the frequency $kR_i$ that is numerically equal to the mode (Fig. 9b,d,f). Fig. 10 shows the
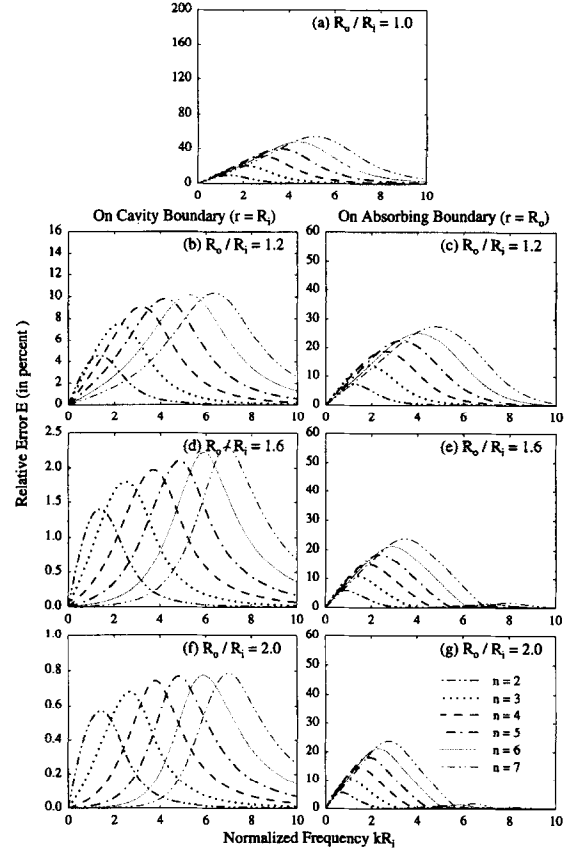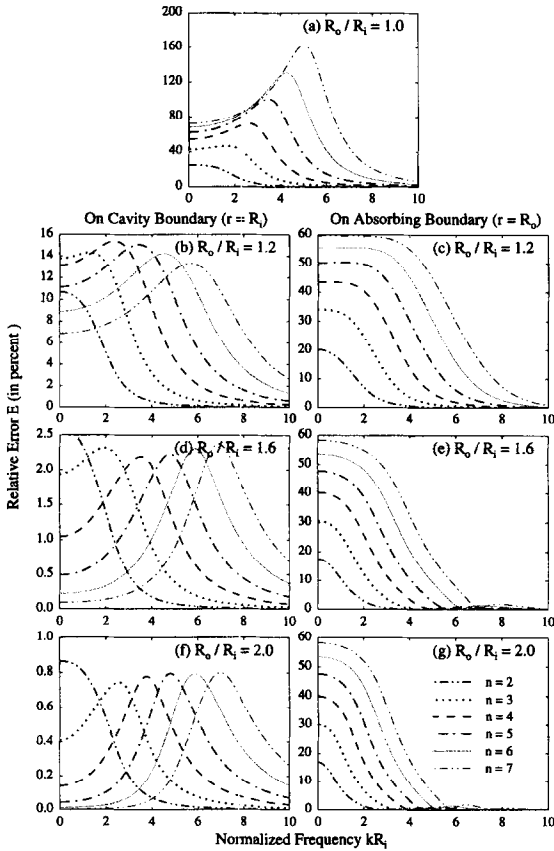
Fig. 9. Relative errors on the cavity and the absorbing boundary as functions of the normalized frequency $kR_i$ due to (19c) with $\gamma = \gamma_0$; various locations $R_o/R_i$.

Fig. 10. Relative errors on the cavity and the absorbing boundary as functions of the normalized frequency $kR_i$ due to (19c) with $\gamma = \gamma_{opt}$; various locations $R_o/R_i$.

corresponding error curves for the second-order condition (19c) with $\gamma = \gamma_{opt}$. While the observations made for Fig. 9 are also valid here, because of the vanishing errors at the zero-frequency limit, the errors are effectively decreased over the entire frequency range. In Fig. 11, the error $E$ on the cavity boundary is plotted against the normalized annulus size $(R_o - R_i)/\lambda$ for different values of $n$ and $kR_i$. All the calculations are for the second-order condition (19c) with $\gamma = \gamma_0$. It can be seen that, in order to limit the error to 5 percent, it is sufficient to place the absorbing boundary at a distance of 0.24 of the wavelength $\lambda$ from the cavity boundary. Notice also that as $n$ increases, errors at the higher frequencies become greater than for the low frequencies for a fixed value of the abscissa. The explanation to this paradox is that for a fixed $(R_o - R_i)/\lambda$ the actual distance $R_o - R_i$ is inversely proportional to the normalized frequency $kR_i$. Thus, for example, a point on the $kR_i = 0.1$ curve corresponds to an actual physical distance of the artificial boundary which is five times greater than the point with the same abscissa on the $kR_i = 0.5$ curve. Hence, in practice, selecting the position of $\Gamma_a$ based on the lower dominant frequencies and lower modes can be expected to give satisfactory results for all frequencies and angular modes.

## 5.2. Finite element analysis

Two sets of problems are considered for assessing the accuracy of the second-order impedance-infinite element corresponding to $\gamma = \gamma_0$. The cavity problem is subjected again to steady-state harmonic excitation and alternatively to transient excitations. In Fig. 12, we compare the exact solution (40) for $kR_i = 1$ to the corresponding finite element solution obtained in conjunction with the impedance-infinite
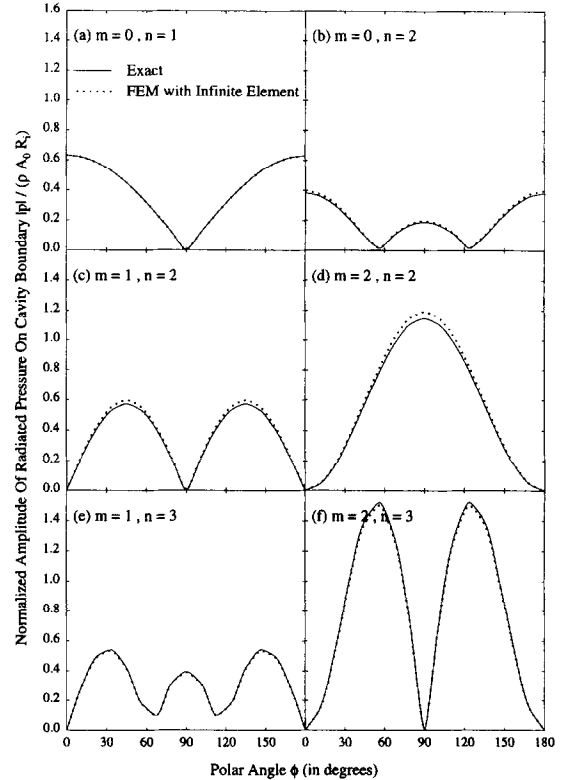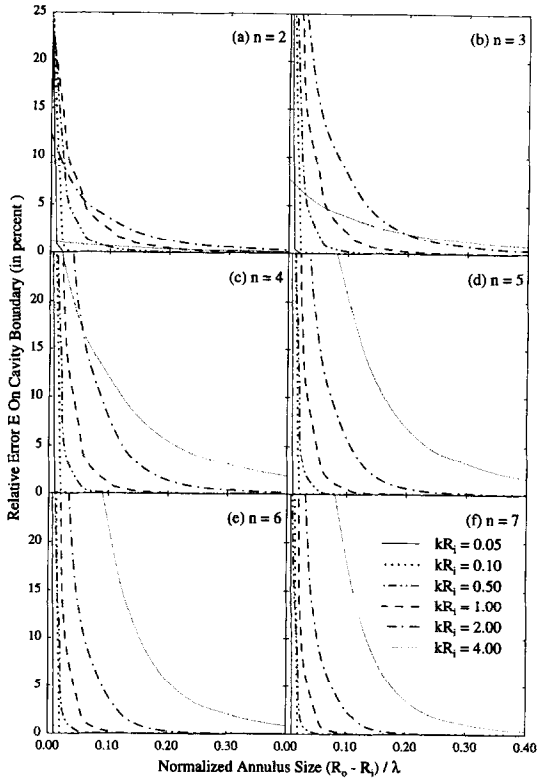
Fig. 11. Relative errors on the cavity boundary as functions of the annulus size $(R_o - R_i)/\lambda$ due to (19c) with $\gamma = \gamma_0$; various harmonics; various frequencies $kR_i$.

Fig. 12. Comparison between exact and FEM solutions along the $\theta = 0°$ meridian; impedance-infinite element at $R_o/R_i = 1.2$; normalized frequency $kR_i = 1$; various harmonics.

element. The finite element results shown are those along the meridian $\theta = 0°$, and for several values of the pair $m$, $n$ which characterizes the tesseral harmonics. The impedance-infinite element was placed at $R_o = 1.2R_i$; eight-noded (hexahedra) isoparametric elements were used for representing the interior of the acoustic fluid, and four-noded isoparametric quadrilateral elements were used for the impedance-infinite element on the absorbing surface; five radial elements were used to span the annular domain, while the traces of 384 elements covered the spherical surfaces. The mesh, typical of our applications, is shown in Fig. 13 for only half of the annular spherical domain; the exterior surface of the mesh is covered with impedance-infinite elements. As can be seen in Fig. 12 the agreement between the depicted exact and finite element solutions is excellent. We remark that the finite element solutions were obtained with a commercial code (ANSYS) modified especially in order to accommodate the impedance-infinite element.

Fig. 14 presents a comparison between the real and imaginary parts of the finite element and exact solutions for a frequency sweep in the range between $kR_i = 1$ to $kR_i = 20$ and for the same spherical geometry as before (Fig. 4), using the same mesh as before. The results shown are for the pair of the tesseral harmonics $m = 2$, $n = 2$. The agreement between the two solutions is excellent. The location of the absorbing boundary was kept constant during the sweep which implies the wide applicability of the impedance-infinite element since it was placed at distances that varied between 0.03 of the wavelength for the lowest frequency to 0.64 for the highest frequency.

As an example of the applicability of the impedance-infinite element in the time-domain, we consider next the transient response of the cavity problem when a rectangular pulse excitation is applied on its boundary, i.e. when
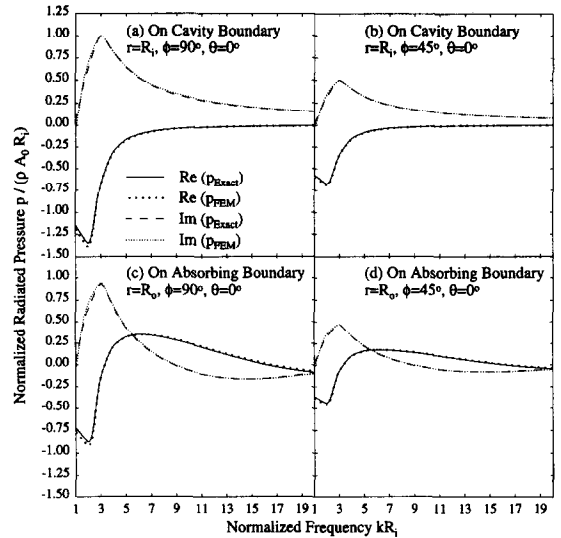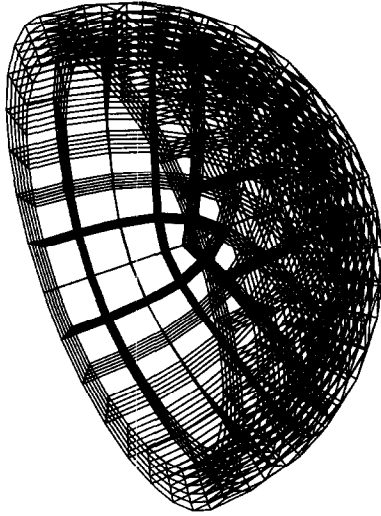
Fig. 13. Typical mesh used in radiation problems.

Fig. 14. Comparison between exact and FEM solutions; impedance-infinite element at $R_o/R_i = 1.2$; $m = 2$, $n = 2$.

$$p_r = \rho A_0 [H(t) - H(t - R_i/c)] P_n^{(m)}(\cos \phi) \cos m\theta \ , \quad \text{at } r = R_i \ ,  \tag{44}$$

in which $H(t)$ is the Heaviside step pulse. This excitation represents a severe test for the impedance-infinite element since it contains large low-frequency contributions, including a strong zero-frequency component. In Fig. 15 we compare the radiated pressure obtained directly in the time-domain using the impedance-infinite element (dashed line) with the transient solution obtained by transforming the exact analytical response (41a) in the frequency-domain in the time-domain via the FFT. Also shown are finite element solutions obtained directly in the time-domain by using the first-order condition and the zeroth-order condition (19a). In all cases the approximate results were obtained by placing the absorbing surface at $R_o = 1.5R_i$; 15 radial and 384 circumferential elements were used. The numerical solutions were carried out using the standard trapezoidal rule for integrating the equations of motion in time with a time step of $\Delta t\, c/R_i = 0.05$. In all cases, the agreement between the solutions obtained with the impedance-infinite element and the exact ones is very good; there are significant discrepancies resulting from the use of either of the other two conditions, especially the plane wave approximation (19a).

Thus far, we have considered problems characterized by spherical geometries in an effort to provide comparisons with existing exact solutions. In order to illustrate the applicability of the finite element/impedance-infinite element methodology to more general geometries, we consider now the scattering of a steady-state harmonic plane wave by a cubic rigid scatterer and compare the scattering patterns to those generated by a spherical rigid scatterer. Let the incoming plane wave be denoted by $p^0$. Then

$$p^0 = P^0\, e^{i(kx + \omega t)} \ , \tag{45}$$

represents a plane wave traveling towards the negative $x$ axis with an amplitude of $P^0$. The existence of a rigid boundary implies zero fluid velocity along the direction normal to the scatterer's surface at the interface between the scatterer and the fluid, and hence, by virtue of the continuity relation, the normal derivative of the total pressure on the interface is zero. If the scattered pressure is denoted by $p^{sc}$ and the total pressure by $p^{tot}$, then

$$p_n^{tot} = 0 \quad \text{and} \quad p_n^{sc} = -p_n^0 \quad \text{at the interface} \ . \tag{46}$$

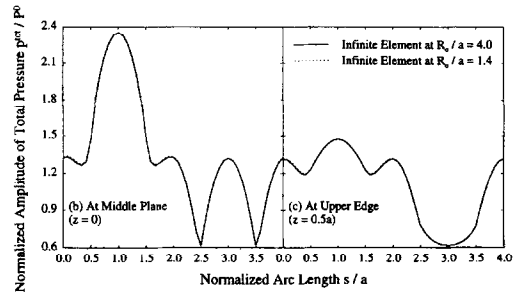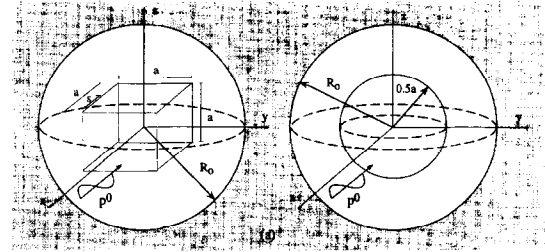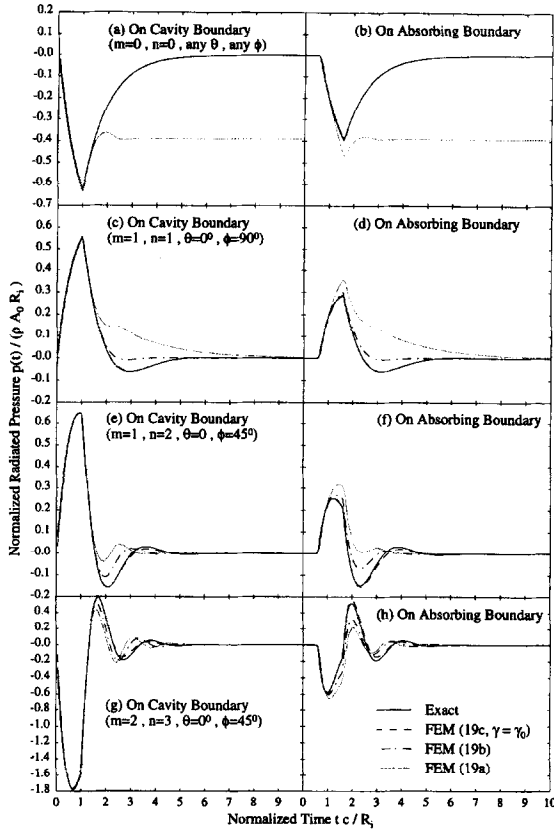Fig. 16(a) depicts the geometric characteristics of the two scatterers; the diameter of the spherical

Fig. 15. Transient response due to a square-pulse excitation of duration $tc/R_i = 1$; absorbing boundary at $R_o/R_i = 1.6$; various absorbing conditions; various harmonics.

Fig. 16. (a) Geometry of spherical and cubic rigid scatterers; (b), (c) comparison between two FEM solutions along the perimeter of the cubic scatterer due to different positions of the absorbing boundary ((19c) with $\gamma = \gamma_0$).

scatterer is equal to the side $a$ of the cubic obstacle. The wavenumber was chosen so that $ka = 3$ for both scatterers. Figs. 16(b,c) show the distribution of the amplitude of the total pressure along two different horizontal paths, on the surface of the cubic scatterer, one on the middle plane ($z = 0$) and the other on the upper edge of the cube ($z = 0.5a$), for two different positions of the absorbing surface. The two traces are practically indistinguishable, thereby indicating that accurate solutions are obtained for this problem by placing the impedance-infinite element as close as $R_o = 1.4a$.

Fig. 17 shows pressure contours for the spherical and cubic rigid scatterers. Figs. 17(a,b) show the normalized scattered pressure patterns, while Figs. 17(c,d) show the normalized total pressure distribution, on a cross section along the middle plane ($z = 0$) of the three-dimensional domain. Finally, Fig. 18 shows the distribution of the normalized total pressure on the surface of a cubic and a spherical scatterer. Once the pressure directly on the scatterer has been established, the pressure anywhere within the fluid can be obtained readily, e.g. by the use of an integral representation.

## 6. Concluding remarks

This paper had two major objectives: (a) to introduce a systematic procedure for constructing artificial boundary conditions for the three-dimensional scalar wave equation, and (b) to present a robust, efficient and accurate methodology based on the finite element method, standard step-by-step time integration, and a new impedance-infinite element that allows for numerical solutions in both the time- and frequency-domains. In light of the excellent agreement between the approximate and exact
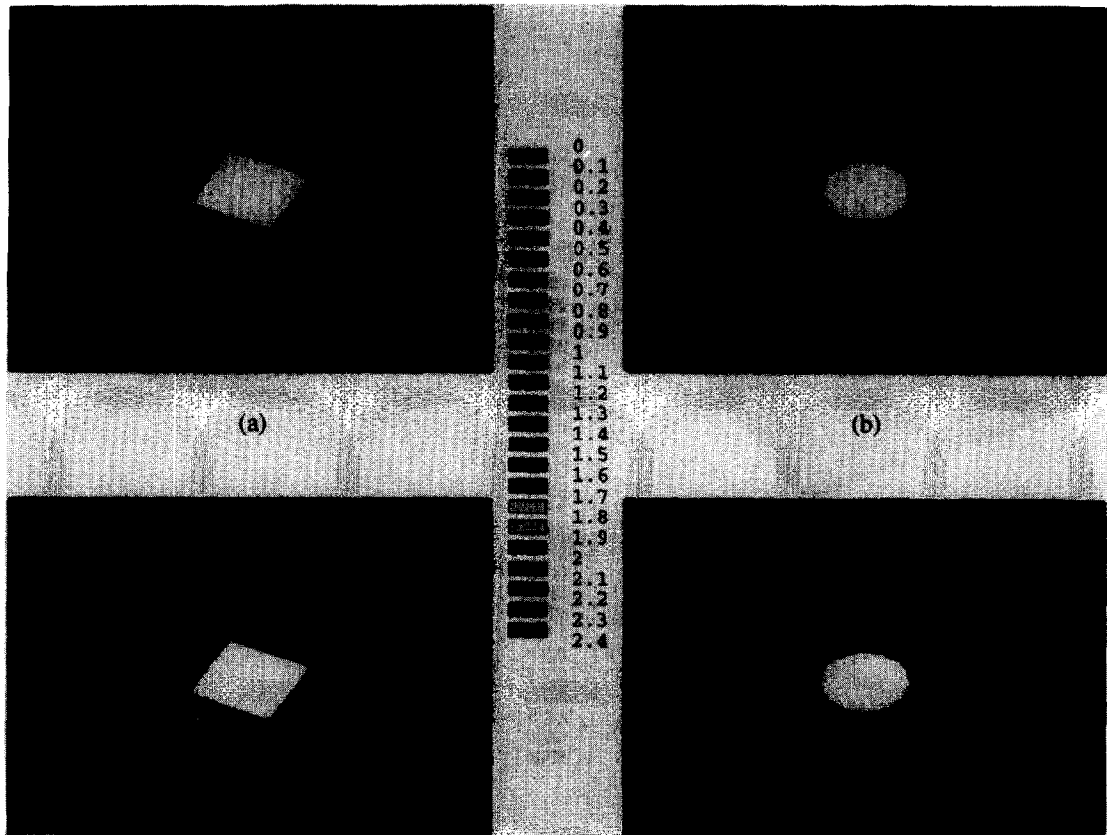
Fig. 17. Normalized pressure distributions on the midsection horizontal plane around rigid cubic and spherical scatterers due to an impinging plane wave; normalized frequency $ka = 3$; (a), (b) scattered field (top row); (c), (d) total field (bottom row).

solutions obtained for the test problems, it appears that the proposed methodology is a powerful tool for solving accurately and efficiently problems in structural acoustics involving complex interior structures.

The new impedance-infinite element permits one to retain the familiar form of the discretized equations of motion with their sparsity and symmetry intact. Since the element is completely represented by a pair of local, symmetric, frequency-independent, stiffness and damping matrices, the entire procedure lends itself to easy incorporation into existing finite element codes for interior problems. It also allows for ready parallelization that will best exploit the main features of particular advanced architectures.

In this paper we have obtained results using the impedance-infinite element on a spherical artificial boundary. It is anticipated that further economy of the computational domain will result from the use of an ellipsoidal artificial boundary.
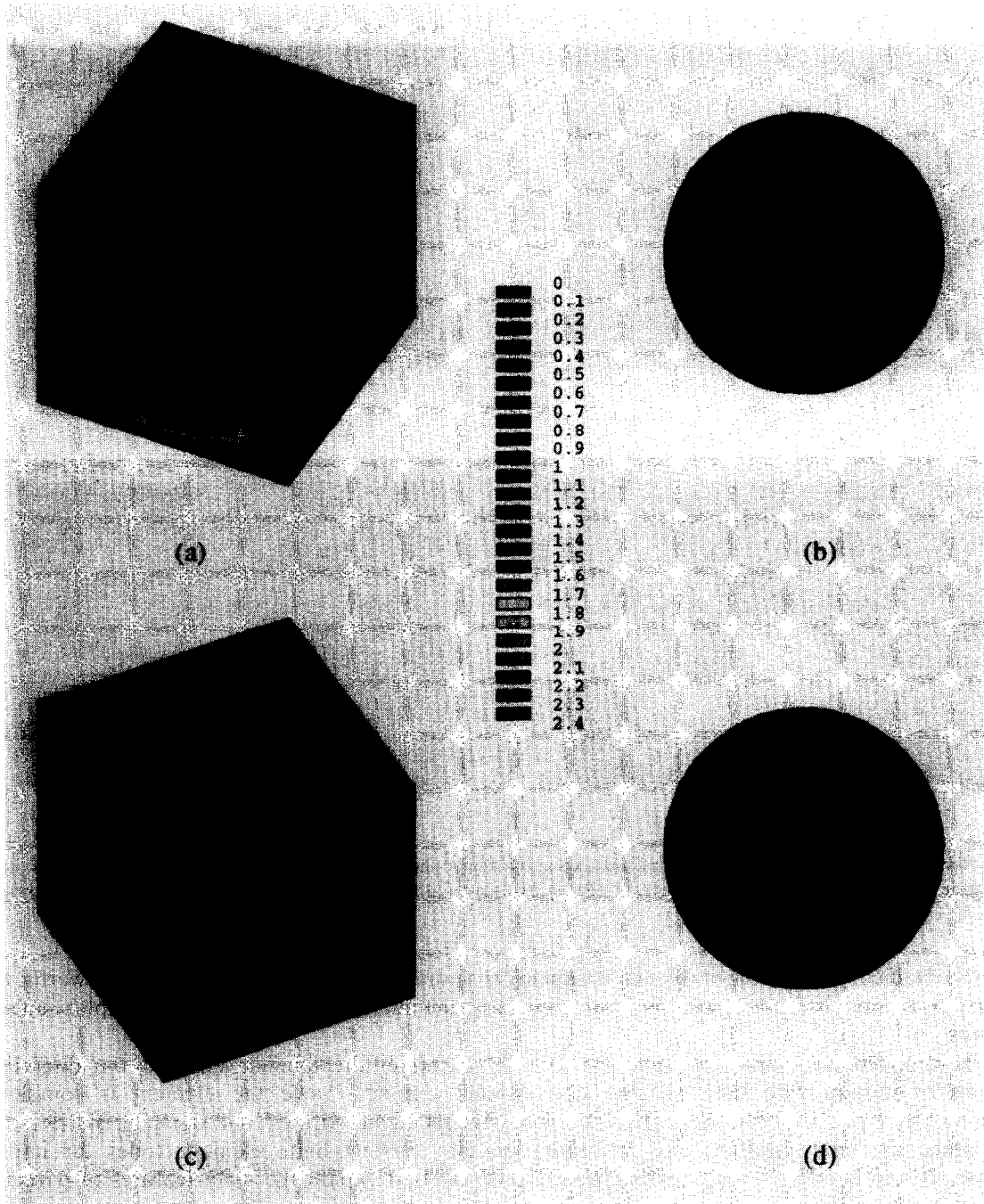
## Acknowledgment

Fig. 18. Normalized total pressure distributions on the surface of rigid cubic and spherical scatterers due to an impinging plane wave; normalized frequency $ka = 3$; (a), (b) back-scattered region (top row); (c), (d) forward-scattered region (bottom row).

## Appendix A

In this appendix we provide a proof for (6a), i.e. we show that

$$\hat{p}(x, s) = \int_0^\infty e^{-st} \hat{P}(x, s; t) \, dt, \quad x \in \bar{\Omega}^+ , \tag{A.1}$$

is indeed a solution to the following initial and boundary value problem for the exterior wave equation:

$$\ddot{p}(x, t) = c^2 \Delta p(x, t) , \quad x \in \Omega^+ , \quad t \geq 0 , \tag{A.2a}$$

$$p(x, t) = \hat{P}(x, s; t) , \quad x \in \Gamma_a , \quad t > 0 , \tag{A.2b}$$

$$p(x, 0) = 0 , \quad \dot{p}(x, 0) = 0 , \quad x \in \bar{\Omega}^+ . \tag{A.2c}$$

To this end, we consider the same problem (A.2) with, however, a unit step function as the Dirichlet datum on $\Gamma_a$. Accordingly, let $q(x, t)$ by the solution to

$$\ddot{q}(x, t) = c^2 \Delta q(x, t) , \quad x \in \Omega^+ , \quad t \geq 0 , \tag{A.3a}$$

$$q(x, t) = 1 , \quad x \in \Gamma_a , \quad t > 0 , \tag{A.3b}$$

$$q(x, 0) = 0 , \quad \dot{q}(x, 0) = 0 , \quad x \in \bar{\Omega}^+ . \tag{A.3c}$$

Then, by direct application of Duhamel's principle [7], one obtains

$$[p(x, t)]_{x \in \bar{\Omega}^+} = [q(x, 0)]_{x \in \bar{\Omega}^+} [\hat{P}(x, s; t)]_{x \in \Gamma_a}$$
$$+ \int_0^t [\hat{P}(x, s; t)]_{x \in \Gamma_a} \left[ \frac{\partial q(x, t - \tau)}{\partial t} \right]_{x \in \bar{\Omega}^+} d\tau . \tag{A.4}$$

Application of the Laplace transform on (A.4), while taking into account the initial conditions (A.3c), leads to

$$\hat{p}(x, s) = s[\hat{q}(x, s)]_{x \in \bar{\Omega}^+} + \int_0^t e^{-st} [\hat{P}(x, s; t)]_{x \in \Gamma_a} dt$$
$$= \int_0^t e^{-st} [s[\hat{q}(x, s)]_{x \in \bar{\Omega}^+} + [\hat{P}(x, s; t)]_{x \in \Gamma_a}] dt$$
$$\equiv \int_0^t e^{-st} [\hat{P}(x, s; t)]_{x \in \bar{\Omega}^+} dt , \tag{A.5}$$

where we define

$$[\hat{P}(x, s; t)]_{x \in \bar{\Omega}^+} = s[\hat{q}(x, s)]_{x \in \bar{\Omega}^+} [\hat{P}(x, s; t)]_{x \in \Gamma_a} . \tag{A.6}$$

Notice that (A.6) holds also for $x$ on $\Gamma_a$, since, by virtue of (A.3b), $\hat{q}(x, s) = 1/s$ on $\Gamma_a$. Eq. (A.5) completes the proof. Alternatively, it can also be seen, by inspection, that (A.1) (or (6a)) satisfies the field equation (4) and the boundary condition (5b).

## Appendix B

The components $g_{ij}$ of the Euclidean metric tensor and the determinant $g$ with elements $g_{ij}$ that characterize the transformation from a cartesian coordinate system to the coordinate system defined by (13), are given as

$$g_{11} = \mathbf{R}_u \cdot \mathbf{R}_u = E - 2\xi L + \xi^2 (2HL - KE) , \tag{B.1a}$$

$$g_{12} = g_{21} = \mathbf{R}_u \cdot \mathbf{R}_w = F - 2\xi M + \xi^2 (2HM - KF) , \tag{B.1b}$$

$$g_{22} = \mathbf{R}_w \cdot \mathbf{R}_w = G - 2\xi N + \xi^2 (2HN - KG) , \tag{B.1c}$$

$$g_{33} = \mathbf{R}_\xi \cdot \mathbf{R}_\xi = 1 , \tag{B.1d}$$

$$g_{13} = g_{31} = \mathbf{R}_u \cdot \mathbf{R}_\xi = 0 , \tag{B.1e}$$

$$g_{23} = g_{32} = \mathbf{R}_w \cdot \mathbf{R}_\xi = 0 , \tag{B.1f}$$

$$g = |g_{ij}| = (EG - F^2)(\xi^2 K - 2\xi H + 1)^2 , \tag{B.1g}$$

where $K$ and $H$ are the Gaussian and mean curvature of $\Gamma_a$, respectively. We use the customary notation for the coefficients of the first and second fundamental forms of the parametric representation of $\Gamma_a$, namely the triplets $E$, $F$, $G$ and $L$, $M$, $N$, respectively. They are defined by

$$E = X_u \cdot X_u , \qquad F = X_u \cdot X_w , \qquad G = X_w \cdot X_w , \tag{B.2a}$$

$$L = -X_u \cdot \nu_u , \qquad M = -\frac{1}{2}(X_u \cdot \nu_w + X_w \cdot \nu_u) , \qquad N = -X_w \cdot \nu_w , \tag{B.2b}$$

$$H = \frac{EN + GL - 2FM}{2(EG - F^2)} , \qquad K = \frac{LN - M^2}{EG - F^2} . \tag{B.2c}$$

In deriving (B.1) we also made use of

$$\nu_u \cdot \nu_u = 2HL - KE , \qquad \nu_u \cdot \nu_w = 2HM - KF , \qquad \nu_w \cdot \nu_w = 2HN - KG . \tag{B.3}$$

In all of the above subscripts $u$, $w$ and $\xi$ denote the corresponding partial derivatives. Notice, that for $\xi = 0$, (B.1a,b,c,g) reduce to

$$g_{11}\big|_{\xi=0} = h_{11} = E , \qquad g_{12}\big|_{\xi=0} = h_{12} = F , \qquad g_{22}\big|_{\xi=0} = h_{22} = G , \qquad g\big|_{\xi=0} = h = EG - F^2 . \tag{B.4}$$

It can be further shown that for any scalar field $\Phi$ one has

$$\nabla\Phi = \frac{1}{g}(g_{22}\Phi_u - g_{12}\Phi_w)R_u + \frac{1}{g}(-g_{12}\Phi_u + g_{11}\Phi_w)R_w + \Phi_\xi R_\xi , \tag{B.5a}$$

$$\Delta\Phi = \frac{1}{\sqrt{g}}\left\{\left[\frac{1}{\sqrt{g}}(g_{22}\Phi_u - g_{12}\Phi_w)\right]_u + \left[\frac{1}{\sqrt{g}}(-g_{12}\Phi_u + g_{11}\Phi_w)\right]_w + [\sqrt{g}\Phi_\xi]_\xi\right\} . \tag{B.5b}$$

By virtue of (B.5a) and the definition (13) the following also holds true:

$$\Phi_\nu = \nabla\Phi \cdot \nu = \Phi_\xi . \tag{B.6}$$

We remark that $\Gamma_a$ is oriented such that $H < 0$, $\forall x \in \Gamma_a$; notice also that $K > 0$, $\forall x \in \Gamma_a$ since $\Gamma_a$ is convex by definition. For these values of $K$ and $H$ it can be shown that the second term in the right-hand side of (B.1g) has no real zeroes for $\xi \geq 0$. Therefore, the zeroes of the determinant $g$ correspond only to the singularity points of $\Gamma_a$ (and to the singularity points of all the surfaces parallel to $\Gamma_a$ within $\Omega^+$) (Fig. 1b). If, for example, $\Gamma_a$ is a sphere and spherical coordinates are used for its parametric representation, then $g$ is zero at the poles.

Finally, if $\nabla^s$ denotes the surface gradient on $\Gamma_a$ then

$$\nabla^s\Phi = \frac{1}{h}(h_{22}\Phi_u - h_{12}\Phi_w)X_u + \frac{1}{h}(-h_{12}\Phi_u + h_{11}\Phi_w)X_w . \tag{B.7}$$

## Appendix C

The radial component $Q_{\mathrm{ex}}$ in (40) is given by

$$Q_{\mathrm{ex}} = \frac{h_n^{(2)}(kr)}{nh_n^{(2)}(kR_i) - kR_ih_{n+1}^{(2)}(kR_i)} , \tag{C.1}$$

where $h_n^{(2)}$ is the spherical Hankel function of the second kind and of $n$th order. Similarly, the radial component $Q_{\mathrm{app}}^{(j)}$ in (41) is given as

$$Q_{\mathrm{app}}^{(j)} = \frac{B_2^{(j)}h_n^{(1)}(kr) - B_1^{(j)}h_n^{(2)}(kr)}{C_1B_2^{(j)} - C_2B_1^{(j)}} , \tag{C.2a}$$

where the coefficients $B_\alpha^{(j)}$, $C_\alpha$ for $\alpha = 1, 2$ are given as

$$C_\alpha = n h_n^{(\alpha)}(kR_i) - kR_i h_{n+1}^{(\alpha)}(kR_i) , \tag{C.2b}$$

$$B_\alpha^{(0)} = \frac{1}{R_o} \{ [n h_n^{(\alpha)}(kR_o) - kR_o h_{n+1}^{(\alpha)}(kR_o)] + ikR_o h_n^{(\alpha)}(kR_o) \} , \tag{C.2c}$$

$$B_\alpha^{(1)} = B_\alpha^{(0)} + \frac{1}{R_o} h_n^{(\alpha)}(kR_o) , \tag{C.2d}$$

$$B_\alpha^{(2)} = \frac{1}{R_o^2} \left\{ [n h_n^{(\alpha)}(kR_o) - kR_o h_{n+1}^{(\alpha)}(kR_o)] \left( ikR_o + \frac{\gamma R_o}{c} \right) \right.$$
$$\left. + \left[ -k^2 R_o^2 + i\left( kR_o + \frac{\gamma R_o}{c} \right) + \frac{n(n+1)}{2} + \frac{\gamma R_o}{c} \right] h_n^{(\alpha)}(kR_o) \right\} . \tag{C.2e}$$

$h_n^{(\alpha)}$ is the spherical Hankel function of the $\alpha$th kind and of $n$th order.

# References

[1] J. Assaad, J.-N. Decarpigny, C. Bruneel, R. Bossut and B. Hamonic, Application of the finite element method to two-dimensional radiation problems, J. Acoust. Soc. Am. 94(1) (1993) 562–573.

[2] A. Barry, J. Bielak and R.C. MacCamy, On absorbing boundary conditions for wave propagation, J. Comput. Phys. 79 (1988) 449–468.

[3] A. Bayliss and E. Turkel, Radiation boundary conditions for wave-like equations, Comm. Pure Appl. Math. 33(6) (1980) 707–725.

[4] P. Bettess and J.A. Bettess, Infinite elements for dynamic problems: Part 1, Engrg. Comput. 8 (1991) 99–124.

[5] P. Bettess and J.A. Bettess, Infinite elements for dynamic problems: Part 2, Engrg. Comput. 8 (1991) 125–151.

[6] R. Bossut and J.-N., Decarpigny, Finite element modeling of radiating structures using dipolar damping elements, J. Acoust. Soc. Am. 86(4) (1989) 1234–1244.

[7] R. Courant and D. Hilbert, Methods of Mathematical Physics, Vol. II Partial Differential Equations (Wiley Classics Edition, Interscience Publishers, New York, NY, 1989).

[8] J.A. DeRuntz, T.L. Geers and C.A. Felippa, The Underwater Shock Analysis Code (USA-version 3), DNA 5615F (Defense Nuclear Agency, Washington, DC, 1980).

[9] B. Engquist and A. Majda, Absorbing boundary conditions for numerical simulation of waves, Math. Comput. 31(139) (1977) 629–651.

[10] B. Engquist and A. Majda, Radiation boundary conditions for acoustic and elastic wave calculations, Comm. Pure Appl. Math. 32(3) (1979) 313–357.

[11] C.A. Felippa, Top-down derivation of doubly asymptotic approximations for structure–fluid interaction analysis, in: R.P. Shaw et al., eds., Innovative Numerical Analysis for the Engineering Sciences (U.P. of Virginia, Charlottesville, 1980) 79–88.

[12] T.L. Geers, Doubly asymptotic approximations for transient motions of submerged structures, J. Acoust. Soc. Am. 64(5) (1978) 1500–1508.

[13] T.L. Geers and Y. Chi-Lin, Inelastic response of an infinite cylindrical shell to transient acoustic waves, ASME J. Appl. Mech. 56 (1989) 900–909.

[14] T.L. Geers and C.A. Felippa, Doubly asymptotic approximations for vibration analysis of submerged structures, J. Acoust. Soc. Am. 73(4) (1983) 1152–1159.

[15] D. Givoli and J.B. Keller, A finite element method for large domains, Comput. Methods Appl. Mech. Engrg. 76 (1989) 41–66.

[16] D. Givoli, Non-reflecting boundary conditions: a review, J. Comput. Phys. 94(1) (1991) 1–29.

[17] T. Hagstrom, S.I. Hariharan and R.C. MacCamy, On the accurate long-time solution of the wave equation in exterior domains: asymptotic expansions and corrected boundary conditions, Math. Comput. 63(208) (1994) 507–539.

[18] I. Harari and T.J.R. Hughes, Galerkin/least-squares finite element methods for the reduced wave equation with non-reflecting boundary conditions in unbounded domains, Comput. Methods Appl. Mech. Engrg. 98 (1992) 411–454.

[19] C.-C. Hsiung, A First Course in Differential Geometry (John Wiley & Sons, Inc. New York, NY, 1981).

[20] D.S. Jones, An approximate boundary condition in acoustics, J. Sound Vib. 121(1) (1988) 37–45.

[21] L.F. Kallivokas, J. Bielak and R.C. MacCamy, Symmetric local absorbing boundaries in time and space, ASCE J. Engrg. Mech. 117(9) (1991) 2027–2048.

[22] L.F. Kallivokas and J. Bielak, Time-domain analysis of transient structural acoustics problems based on the finite element method and a novel absorbing boundary element, J. Acoust. Soc. Am. 94(6) (1993) 3480–3492.

[23] L.F. Kallivokas and J. Bielak, An element for the analysis of transient exterior fluid–structure interaction problems using the FEM, Finite Elem. Anal. Des. 15 (1993) 69–81.

[24] L.F. Kallivokas, Absorbing boundaries conditions and finite elements for transient and harmonic steady-state acoustic fluid-structure interaction, Thesis presented to Carnegie Mellon University, Pittsburgh, PA, in particular fulfillment of the requirements for the degree of Doctor of Philosophy, 1994.

[25] L.F. Kallivokas and J. Bielak, A time-domain impedance element for FEA of axisymmetric exterior structural acoustics, ASME J. Vib. Acoust. 117 (1995) 145–151.

[26] E. Kausel, Local transmitting boundaries, ASCE J. Engrg. Mech. 114(6) (1988) 1011–1027.

[27] G.A. Kriegsmann, A. Taflove and K.R. Umashankar, A new formulation of electromagnetic wave scattering using an on-surface radiation boundary condition approach, IEEE Trans. Antennas Propag. AP-35(2) (1987) 153–160.

[28] L.E. Malvern, Introduction to the Mechanics of a Continuous Medium (Prentice-Hall, Inc., Englewood Cliffs, NJ, 1969).

[29] R.D. Mindlin and H.H. Bleich, Response of an elastic cylindrical shell to a transverse, step shock wave, ASME J. Appl. Mech. 20 (1953) 189–195.

[30] B. Nicolas-Vullierme, A contribution to doubly asymptotic approximations: an operator top-down approach, Numerical Techniques in Acoustic Radiation, NCA-Vol. 6 (ASME, New York, 1989) 7–13.

[31] P.M. Pinsky and N.N. Abboud, Transient finite element analysis of the exterior structural acoustics problem, ASME J. Vib. Acoust. 122 (1990) 245–256.

[32] P.M. Pinsky and N.N. Abboud, Finite element solution of the transient exterior structural acoustics problem based on the use of radially asymptotic boundary operators, Comput. Methods Appl. Mech. Engrg. 85 (1991) 311–348.

[33] P.M. Pinsky, L.L. Thompson and N.N. Abboud, Local high-order radiation boundary conditions for the two-dimensional time-dependent structural acoustics problem, J. Acoust. Soc. Am. 91(3) (1992) 1320–1335.

[34] O.C. Zienkiewicz and P. Bettess, Infinite elements in the study of fluid structure interaction problems, Proc. 2nd Int. Symp. Comp. Methods Appl. Sci., Versailles, 1975.